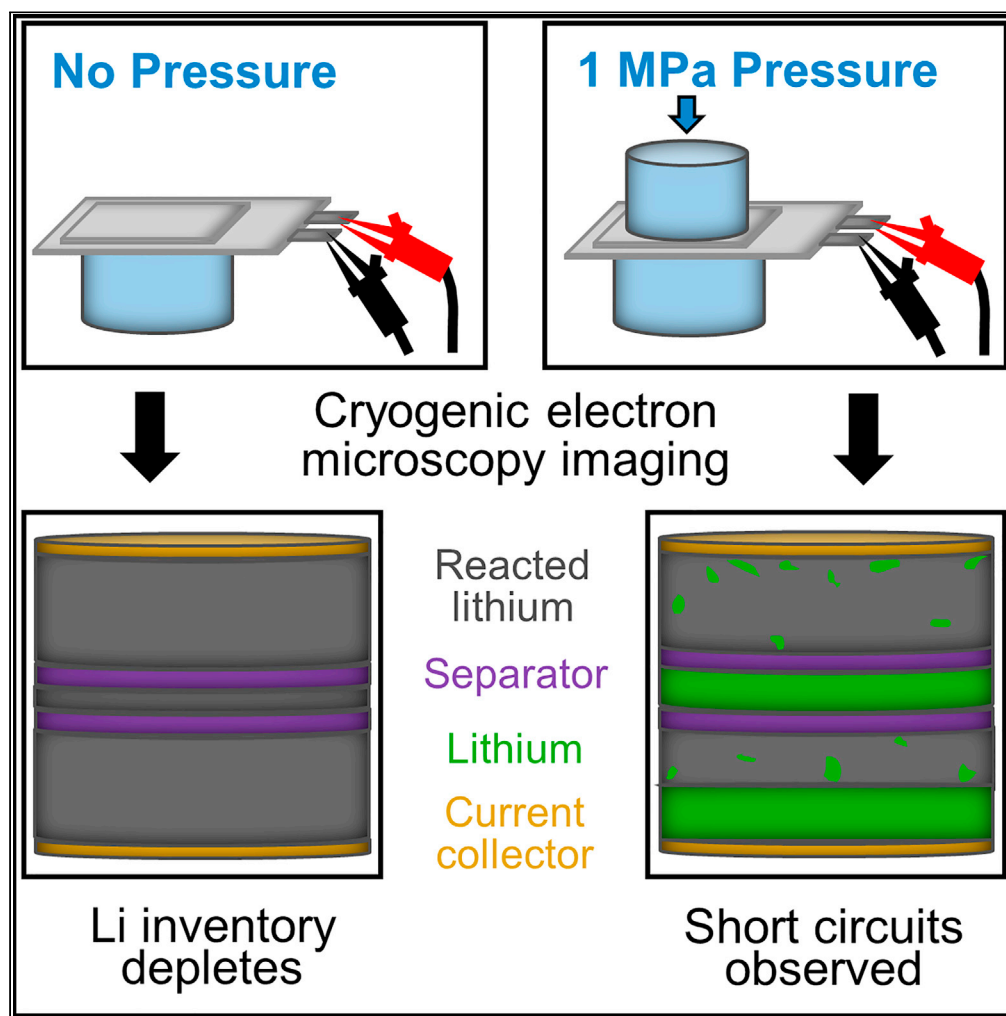**Article**

# Cryogenic electron microscopy reveals that applied pressure promotes short circuits in Li batteries



Katharine L. Harrison, Laura C. Merrill, Daniel Martin Long, ..., Stephen J. Harris, Daniel L. Perry, Katherine L. Jungjohann

katharr@sandia.gov

**Highlights**

Pressure improves Li inventory retention in Li metal batteries at high current

Varying pressure from 0.1 to 1 MPa has little impact on Li morphology at high current

Pressure promotes short circuits in Li metal batteries at high current

Use of two separators in Li metal batteries masks short circuits

## Article

# Cryogenic electron microscopy reveals that applied pressure promotes short circuits in Li batteries

Katharine L. Harrison,[1,10,*] Laura C. Merrill,[1] Daniel Martin Long,[2] Steven J. Randolph,[5,7] Subrahmanyam Goriparti,[1,8] Joseph Christian,[5] Benjamin Warren,[1] Scott A. Roberts,[3] Stephen J. Harris,[6] Daniel L. Perry,[4] and Katherine L. Jungjohann[2,9]

## SUMMARY

**Li metal anodes are enticing for batteries due to high theoretical charge storage capacity, but commercialization is plagued by dendritic Li growth and short circuits when cycled at high currents. Applied pressure has been suggested to improve morphology, and therefore performance. We hypothesized that increasing pressure would suppress dendritic growth at high currents. To test this hypothesis, here, we extensively use cryogenic scanning electron microscopy to show that varying the applied pressure from 0.01 to 1 MPa has little impact on Li morphology after one deposition. We show that pressure improves Li density and preserves Li inventory after 50 cycles. However, contrary to our hypothesis, pressure *exacerbates* dendritic growth through the separator, *promoting* short circuits. Therefore, we suspect Li inventory is better preserved in cells cycled at high pressure *only* because the shorts carry a larger portion of the current, with less being carried by electrochemical reactions that slowly consume Li inventory.**

## INTRODUCTION

Although Li metal anode batteries theoretically could enable 2–5x improvements in pack level energy density (Eroglu et al., 2015), they are plagued with practical challenges that encumber their commercialization. Practical energy density gains require Li metal anodes that can cycle efficiently at high gravimetric and volumetric capacities and at high current densities (Tarascon and Armand, 2001; Gallagher et al., 2014; Eroglu et al., 2015; Mikhaylik et al., 2010; Liu et al., 2019). Li is generally unstable in liquid electrolytes, so a solid electrolyte interphase (SEI) passivation layer forms on contact with the electrolyte and then grows during cycling. The SEI reaction consumes Li and electrolyte, increases impedance, and leads to volume expansion of the Li deposits. Li metal tends to deposit in mossy or dendritic high aspect ratio morphologies (Frenck et al., 2019; Ding et al., 2013; Zachman et al., 2018), particularly at high currents, which can lead to safety problems such as short circuits and fires. Such morphologies also exacerbate parasitic reactions due to their large surface areas, which enables significant parasitic SEI growth. Because of their theoretical promise, the research community has invested heavily in overcoming challenges (Kim et al., 2013; Lin et al., 2017) with Li anodes including (1) electrolyte additives (Ding et al., 2014; Zhang, 2006; Jozwiuk et al., 2016) and new electrolytes (Qian et al., 2015; Han et al., 2011; Ding et al., 2013; Naoi et al., 1999), (2) artificial SEI coatings to better control morphological evolution (Kozen et al., 2015; Aetukuri et al., 2015; Li et al., 2015; Zheng et al., 2014; Harrison et al., 2017), (3) periodic high rate cycling to promote self-heating and destruction of dendrites (Li et al., 2018), (4) separator coatings to redirect dendrite growth (Liu et al., 2017), (5) solid state electrolytes that provide a physical barrier to Li dendrites and are often less reactive with Li (Takada, 2013; Sun et al., 2017), and (6) applied interfacial pressure in cells with liquid (Mikhaylik et al., 2010; Hirai et al., 1994a, 1994b; Wilkinson et al., 1991; Wilkinson and Wainwright, 1993; Ota et al., 2004; Weber et al., 2019; He et al., 2019; Harrison et al., 2017, 2021; Louli et al., 2019, 2020; Niu et al., 2019; Yin et al., 2018; Gireaud et al., 2006; Wang et al., 2021; Peabody and Arnold, 2011; Kanamori et al., 2020) and solid electrolytes (Zhang et al., 2020; Wang et al., 2019; Krauskopf et al., 2019; Verma et al., 2021).

Although applied interfacial pressure is often unquantified, it can significantly impact performance in conventional Li-ion batteries (Mussa et al., 2018; Cannarella and Arnold, 2014; Zhao et al., 2017;

[1]Nanoscale Sciences, Sandia National Laboratories, Albuquerque, NM 87123, USA

[2]Center for Integrated Nanotechnologies, Sandia National Laboratories, Albuquerque, NM 87123, USA

[3]Thermal/Fluid Component Science, Sandia National Laboratories, Albuquerque, NM 87123, USA

[4]Materials Characterization and Performance, Sandia National Laboratories, Albuquerque, NM 87123, USA

[5]Materials & Structural Analysis Division, Thermo Fisher Scientific, Hillsboro, OR 97124, USA

[6]Materials Science Division, Lawrence Berkeley National Laboratory, Berkeley, CA 94720, USA

[7]Present address: Nanofabrication Research Laboratory, Center for Nanophase Materials Sciences, Oak Ridge National Laboratory, Oak Ridge, TN 37830, USA

[8]Present address: Happy Electron Lab Inc., Redwood City, CA 94063, USA

[9]Present address: Analytical Microscopy and Imaging Sciences Group, National Renewable Energy Laboratory, Golden, CO80401, USA

[10]Lead contact

*Correspondence:
katharr@sandia.gov

https://doi.org/10.1016/j.isci.2021.103394

Bach et al., 2016; Rubino et al., 2001; Klett et al., 2014; Petzl et al., 2015; Nadimpalli et al., 2015) and Li metal anode batteries (Mikhaylik et al., 2010; Hirai et al., 1994a, 1994b; Wilkinson et al., 1991; Wilkinson and Wainwright, 1993; Ota et al., 2004; Weber et al., 2019; He et al., 2019; Harrison et al., 2017, 2021; Louli et al., 2019, 2020; Niu et al., 2019; Yin et al., 2018; Gireaud et al., 2006; Wang et al., 2019, 2021; Zhang et al., 2020; Krauskopf et al., 2019; Verma et al., 2021; Peabody and Arnold, 2011; Kanamori et al., 2020). Pressure can have a particularly strong impact on Li metal anodes because Li is a soft metal (Fincher et al., 2020) and deposits in compressible and high aspect ratio porous morphologies. Pressure impacts on Li anode cycling have been studied in a variety of liquid electrolytes (Mikhaylik et al., 2010; Hirai et al., 1994a, 1994b; Wilkinson et al., 1991; Wilkinson and Wainwright, 1993; Ota et al., 2004; Weber et al., 2019; He et al., 2019; Harrison et al., 2017, 2021; Louli et al., 2019, 2020; Niu et al., 2019; Yin et al., 2018; Gireaud et al., 2006; Wang et al., 2021; Peabody and Arnold, 2011; Kanamori et al., 2020) and the specific electrolyte formulation impacts the degree to which pressure affects performance (Hirai et al., 1994a; Louli et al., 2019; Weber et al., 2019; Niu et al., 2019; Wang et al., 2021). Pressure can enable dense morphology by constraining growth (Mikhaylik et al., 2010; Hirai et al., 1994b; Wilkinson and Wainwright, 1993) and promoting the reconnection of disconnected, mossy Li, which leads to improved Coulombic efficiency (CE) (Wilkinson and Wainwright, 1993; Hirai et al., 1994b). Denser deposits may also result from a mechanical overpotential that develops in high pressure areas on electrodes (Zhang et al., 2019), with higher pressure regions caused by local growth inhomogeneity or roughness. This overpotential arises because displacing a pressurized interface requires work, and more work is required to continue growth at an asperity already under high local pressure than in a low-pressure region. Therefore, the mechanical overpotential discourages continued growth at asperities and smooths out morphology (Zhang et al., 2019). Finally, applied pressure may also affect Li material properties by inducing creep (Zhang et al., 2020) and residual strain (Rodriguez et al., 2020; Campbell et al., 2018; Lu et al., 2018; Kushima et al., 2017; Cho et al., 2020; Herbert et al., 2018) or by influencing SEI reactions (Harrison et al., 2017).

Motivated to understand the effects of pressure in an electrolyte with high CE, long cycle life, and favorable deposition morphology, we have previously studied varied pressure in the promising electrolyte 4 M lithium bis(fluorosulfonyl)imide in 1,2-dimethoxyethane (4 M LiFSI in DME) (Harrison et al., 2017, 2021). Despite its high viscosity which leads to lower ionic conductivity than conventional lower concentration electrolytes, 4 M LiFSI in DME cycles efficiently and has been previously shown to support high current density (Qian et al., 2015). After demonstrating proof-of-concept that pressure improves morphology in 4 M LiFSI in DME (Harrison et al., 2017), we then systematically studied the effects of 0–10 MPa of pressure on Li cycling and morphology at a low current density of 0.5 mA/cm$^2$ (Harrison et al., 2021). We generally found that increased pressure improved cell-to-cell repeatability, CE, and plating morphology from 0 to 1 MPa. We also found that despite dense morphology for cells cycled at 10 MPa, these cells exhibited high overpotential and poor electrochemical performance, which has been previously shown to arise from local pore closure in the separator (Peabody and Arnold, 2011). In our prior study, high fidelity imaging of air- and beam-sensitive Li metal deposits was enabled through cryogenic (cryo) Ga$^+$ focused ion beam (FIB) and cryo scanning electron microscopy (SEM) techniques. Cryo techniques have been shown to be important for preserving Li metal, electrolyte, and SEI components in liquid electrolytes and enabling imaging of solid-liquid interfaces (Zachman et al., 2018, 2020; Lee et al., 2019). Through cryo FIB and SEM techniques, we previously found that pressure greatly impacts the Li deposit morphology, such that the deposits after one deposition at 0 MPa were 5x thicker than at 1 MPa. Additionally, we observed improved morphology at high pressure after 50 cycles with cryo Ga$^+$ FIB and SEM. However, it was very difficult to image deposits after more extensive cycling due to the thickness of the deposits and slow milling rates associated with conventional Ga$^+$ FIB, so we could not easily quantify the thickness of deposits after extended cycling.

We then addressed this problem of slow milling rates in other previous work by using a laser plasma FIB (laser PFIB) developed by Thermo Fisher Scientific and demonstrated that full coin cells can be cross-sectioned to enable imaging of 1 mm wide sections of entire electrode stacks without disassembling coin cells (Jungjohann et al., 2021). The laser PFIB is equipped with a femtosecond laser that is capable of milling rates 15,000x faster than conventional Ga$^+$ FIB, enabling milling through the entire battery stack, including the coin cell cap, in tens of minutes. By coupling a cryo stage with the laser PFIB/SEM, we were able to freeze, cross-section, and image interfaces in Li versus Cu coin cell electrode stacks with liquid electrolytes. Because this technique can quickly mill through the coin cell cases, spacers, and wave springs, it enables imaging of interfaces without having to disassemble the batteries. When electrode materials are relatively thin (few tens of microns) and remain segregated and independent from one another, Ga$^+$ FIB is

an excellent tool for cross-sectioning electrodes and disassembly of the stack layers is not problematic. However, when electrode materials are very thick or when the stack layers interact with one another and become intertwined, laser PFIB cross-sectioning has distinct advantages. For example, imaging without disassembly is important for studying failure mechanisms related to high rate cycling of Li metal anodes because short circuits involve Li dendrites growing into the separator, so disassembly of cells at electrode-separator interfaces for ex-situ imaging can destroy the evidence of these dendrites. In some cells, the stack layers were so well intertwined, that it was not easy to separate the stack at interfaces and we had to actively rip the interfaces apart. Using this cryo laser PFIB/SEM technique, we previously showed that SEI and Li grew into and damaged the separator, eventually shredding the separator to pieces after extended Li versus Cu coin cell cycling in 2.8 M LiFSI in DME (Jungjohann et al., 2021).

Building on our previous work (Harrison et al., 2017, 2021; Jungjohann et al., 2021), we herein describe the effects of pressure on Li cycling in 4 M LiFSI in DME at high current density, which we find differs significantly from effects of pressure we have previously reported at low current density (Harrison et al., 2021). Because high current is known to exacerbate dendritic growth, which is caused by poorly controlled morphology during deposition, we hypothesized that increased pressure may help *mitigate* dendrites through physically constraining them or because pressure should cause more uniform Li growth by generating a mechanical overpotential (Zhang et al., 2019). Instead, we find here through ex-situ cryo $Ga^+$ FIB milling and cryo SEM imaging that pressure impacts morphology only mildly at high current after one Li deposition in the range of 0.01–1 MPa. To enable imaging of Li versus Cu cells after 50 cycles without having to rip apart interfaces and potentially destroy evidence of dendrites, we use cryo laser PFIB milling and cryo SEM imaging to study cells cycled at varied pressures. Imaging reveals that the electrode stacks are generally thinner at higher pressures and the Li inventory remains on the counter electrode only when cells are cycled at 1 MPa. This observation agrees with electrochemical data, which also suggests depletion of excess Li inventory on the counter electrode at lower pressures but not at 1 MPa.

In contrast to our hypothesis that dendrites would be suppressed with applied pressure, we find that pressure actually *exacerbates* Li growth into separators and the formation of soft short circuits. The cryo imaging, combined with impedance and cycling data with one and two separators, further reveals that the use of two separator sheets in cells can delay failure associated with dendritic growth because the Li metal deposits are redirected and accumulate between separator sheets rather than dendrites connecting and shorting to the opposite electrode. While we show that 1 MPa of pressure enables cells to cycle without capacity loss over 50 cycles, we find that *only* cells cycled without pressure (0 MPa applied) show no obvious signs of short circuits in the electrochemical data and less evidence of Li deposits between separator sheets. Because soft short circuits are much more prevalent at high pressure, we suspect that better Li inventory retention at high pressure may only occur because pressure *exacerbates* dendrites and resulting soft short circuits; in turn, the more severe soft shorts enable more current to be carried directly across the shorts, which preserves Li inventory because less current is carried through the electrochemical reactions that are accompanied by parasitic losses.

## RESULTS

### Effects of pressure on Li electrochemistry

To understand the impact of pressure on Li cycling in 4 M LiFSI in DME at the high current of 4 mA/cm$^2$, we cycle Li versus Cu half cells $50\frac{1}{2}$ times in pouch cells with pressures of 0, 0.01, 0.1, 1, and 10 MPa. 0–10 MPa of pressure is selected to be consistent with our previous work and to include pressures similar to ~0.1 MPa in coin cells (Harrison et al., 2021), pressures lower than in coin cells (0 and 0.01 MPa), and pressures above that in coin cells (1 and 10 MPa) but below the yield stress of Li metal, which is approximately 16 MPa (Zhang et al., 2020). It is important to note that although we apply pressure to cells that are mounted on smooth, mirror bright platens to encourage uniformity, inherent interfacial roughness of the cell components and the separator ensure that these applied pressures are only averages and that the actual pressure varies above and below the average applied value with location in accordance with local roughness (Zhang et al., 2019).

Potential versus time data in Figures 1A–1C show that the cells at 0, 0.01, and 0.1 MPa polarize to the −1 V limit on plating after 30–45 cycles. The polarization correlates with a drop in the plating capacity in later cycles, as shown in Figures 1E–1G. Polarization at the end of each plating step likely results from loss of accessible Li inventory during cycling. It is possible that Li inventory may become inaccessible due to
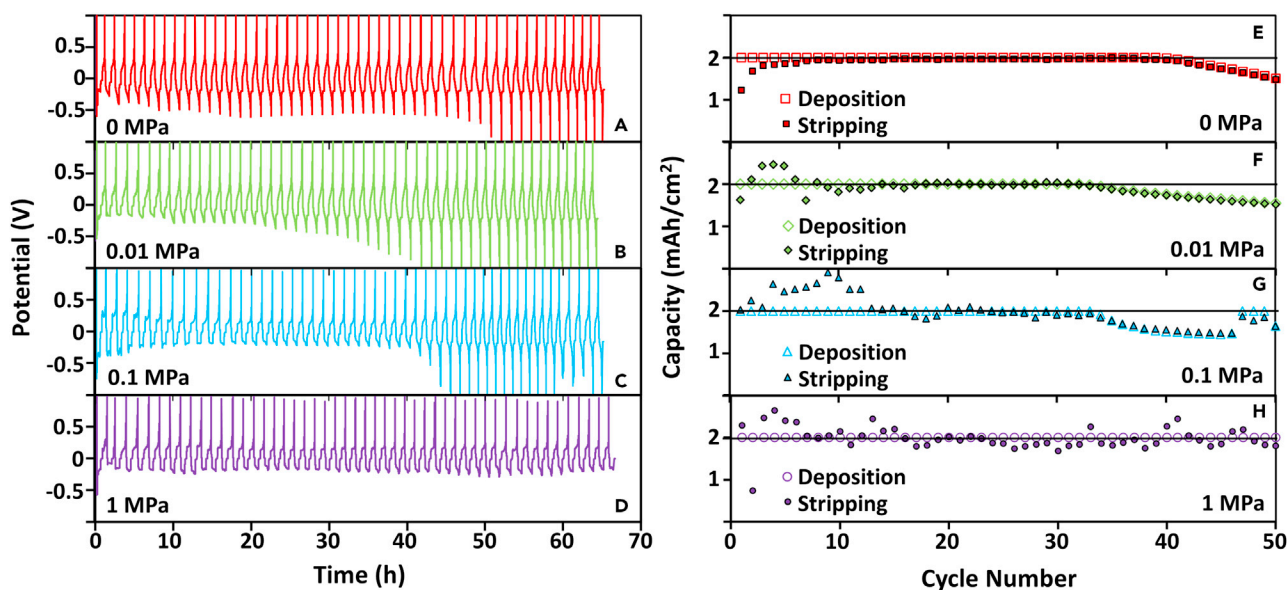
**Figure 1. Electrochemical data for cells cycled at various applied pressures with two separator sheets**
Potential versus time and capacity versus cycle number data for Li versus Cu pouch cells with two sheets of Celgard 2325 separators cycled at 4 mA/cm$^2$ to 2 mAh/cm$^2$ and tested under 0 MPa (A and E), 0.01 MPa (B and F), 0.1 MPa (C and G), and 1 MPa (D and H) of pressure.

impedance rise during cycling as SEI and dead Li accumulate and impede Li transport. Impedance rise would lead to increased polarization; however, if the polarization was occurring due to increased impedance from SEI and dead Li accumulation over many cycles, the increased polarization should occur across the entire plating profile rather than selectively only at the end of the plating step. Figure S1 shows that the profiles before and after the onset of plating capacity loss are nearly identical throughout the plating step, except the voltage suddenly drops before the specified capacity is reached. Therefore, we discount that sudden polarization near the end of each plating step in cycles 30–50 is correlated with transport limitations related to impedance rise from SEI and dead Li accumulation.

Alternatively, Li inventory may become inaccessible because small amounts are converted to SEI and dead Li in each cycle, which accumulates over the range of cycling and equates to gradual consumption of the excess Li reservoir on the counter electrode. These cells employ a thin 50 μm Li counter electrode, which equates to approximately a 5-fold excess relative to the capacity plated in each cycle. The programmed capacity is 2 mAh/cm$^2$ or approximately 10 μm equivalent thickness in each cycle if Li were deposited in a fully dense film. We intentionally use limited Li counter electrodes, as has been recommended by the Li metal anode research community (Liu et al., 2019; Albertus et al., 2018), to elucidate the impact of inefficiency by making cell failure more obvious than with conventional huge excess Li reservoirs at the counter electrode. Recently, it has been demonstrated that limited excess Li cells gradually start losing capacity very early in cycling and eventually fail because, after the excess Li on the counter electrode is consumed, the available Li decreases with each cycle (Liu et al., 2019). Once the excess Li reservoir at the counter electrode is depleted, the counter electrode has no Li left after plating on the working electrode (which corresponds to stripping at the counter electrode). When the excess Li on the counter electrode becomes completely depleted, the only Li inventory in the cell is the Li that was just plated on the working electrode, which is 2 mAh/cm$^2$ in this study. On the next half cycle when Li is stripped from the working electrode and plated back on the counter electrode, the Li plated on the counter electrode is less than 2 mAh/cm$^2$ because there are losses in each cycle. Therefore, in the following half cycle when Li is plated on the working electrode and stripped from the counter electrode, the plated capacity has to be less than the programmed 2 mAh/cm$^2$ because there is no longer 2 mAh/cm$^2$ of accessible Li inventory remaining in the cell.

After the excess reservoir of Li is depleted on the counter electrode, the plated capacity on the working electrode should decrease systematically with every cycle because the counter electrode can no longer compensate for the parasitic losses that occur in each cycle. This systematic drop in plating capacity is

exactly what we observe, so we conclude that the onset of capacity losses in these cells at low pressure correlates with the point in cycling when the counter electrode no longer has excess bulk Li reservoir remaining. Instead, the counter electrode can only supply the amount of Li that was plated on the counter electrode while the working electrode is stripped in the previous half cycle, minus the losses during that half cycle. The CE remains high even when the capacity drops because the Li can still be plated and stripped as efficiently as before the capacity drop; the losses with each cycle can just no longer be compensated for by the excess at the counter electrode. This argument is corroborated by data in Figure S2, which shows that pouch cells fabricated with a large excess of Li on the counter electrode can cycle 50 times at 0 MPa without polarizing to the voltage cutoff during plating and without the systematic drop in capacity observed in Figure 1A for cells with a small Li excess on the counter electrode. As will be discussed in more detail later, imaging in Figure 4 further corroborates this argument by showing that the excess Li reservoir at the counter electrode is visibly depleted in cells that exhibit capacity loss (cells cycled at 0–0.1 MPa) and visibly remains in cells that do not exhibit capacity loss (cells cycled at 1 MPa).

Cycling at higher pressures of 1 and 10 MPa leads to distinctly different behaviors than at lower pressures of 0–0.1 MPa. In contrast to cells cycled at lower pressures, cells cycled at 1 MPa are able to deliver the specified plating capacity for all 50 cycles, as shown in Figure 1H, and do not polarize to the −1 V limit during the plating steps, as shown in Figure 1D. At 10 MPa, we are unable to deposit Li because the cells immediately polarize to the −1 V cutoff limit with very little capacity, as shown in Figure S3. Previously, we studied the effects of pressure at low current (0.5 mA/cm$^2$) and we found that the overpotential increases significantly for cells cycled at 10 MPa relative to 1 MPa (Harrison et al., 2021). We attribute the increased overpotential at low current to transport limitations caused by pore closure in the separator, as a previous study suggested begins to occur between 1 and 10 MPa (Peabody and Arnold, 2011). Our results at 10 MPa are also consistent with another study that showed Li anode cyclability improves with pressure until a limit of between 1.39 and 1.85 MPa, at which point increased pressure degrades performance (Kanamori et al., 2020). Transport is more severely limited at high current due to the need to move Li$^+$ ions more quickly to meet the current density demands, so pore closure resulting from high pressure on the separator should have a more significant impact on Li$^+$ transport and Li plating at high current, which is consistent with our results here that cells cycled at 10 MPa and high current polarize and cannot cycle, even though they could cycle (though poorly) in our previous work at low current. Regardless, cycling with pressure of around 10 MPa leads to poor performance, so 10 MPa will not be discussed further in this work.

Despite improved capacity retention in cells cycled at 1 MPa relative to lower pressures, only cells cycled at 0 MPa, Figure 1E, exhibit stripping capacities that conform to expectations for well-behaved cells. Their stripping capacities begin considerably lower than the plating capacities in early cycles, which is typical and results from irreversible loss of Li inventory during SEI formation and because Li becomes stranded or "dead" (Fang et al., 2019). After the first few cycles, the stripping capacity increases to similar values as the plating capacity, but remains slightly lower, again due to SEI and dead Li that continue to form in small amounts with additional cycling. Finally, plating and stripping capacities drop in unison, which suggests a loss of excess Li reservoir on the counter electrode, as was discussed previously, and indicates that the available Li remaining can be plated and stripped reasonably efficiently (with small continued losses on each cycle).

In contrast to the cells cycled at 0 MPa, cells cycled at increased pressure exhibit scatter in the stripping capacity data shown in Figures 1F–1H with significant regions during cycling, particularly in early cycles, where stripping capacities exceed plating capacities. To confirm that the excess stripping capacity is repeatable in cells cycled at 0.01, 0.1, and 1 MPa, but is never observed at 0 MPa, we present data from several replicate cells in Figures S4–S7. We note that cells cycled at 0.1 MPa exhibit the most variation from cell to cell after capacity loss begins. While all replicates show signs of Li inventory loss by around 40 cycles, the capacity continuously drops in some cells with each cycle, similar to cells cycled at 0 and 0.01 MPa. Other cells cycled at 0.1 MPa exhibit dropping capacity, followed by recovery such that the programmed capacity can be plated again, as shown in Figure 1G at cycle 47. When this capacity recovery occurs, the plating capacity-voltage curve exhibits sudden changes in the overpotential and noisy electrochemical signatures, as shown in Figure S8. Sudden changes and noise in the electrochemistry suggest that stranded Li may be reconnecting near the end of the plating steps or that soft short circuits enable the increased capacity. These topics will be subsequently discussed. Regardless, these cells clearly are not well-behaved or robustly delivering capacity.
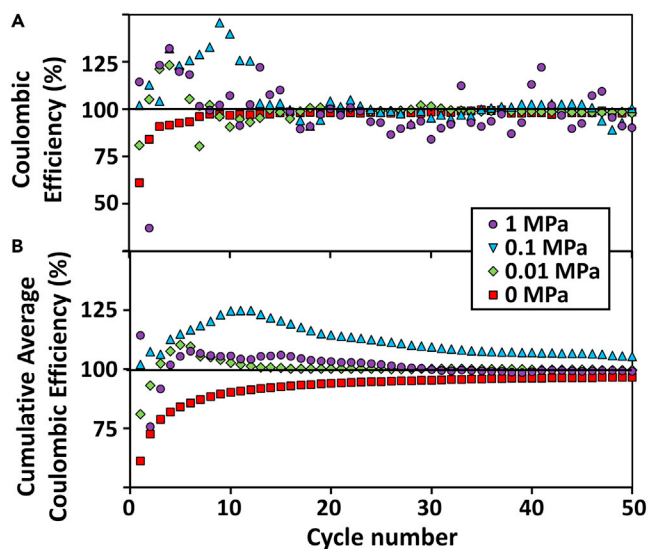
**Figure 2. Coulombic efficiency data for cells cycled at various applied pressures with two separator sheets**
Coulombic efficiency (A) and cumulative average Coulombic efficiency (B) versus cycle number data for Li versus Cu pouch cells with two sheets of Celgard 2325 separators cycled at 4 mA/cm$^2$ to 2 mAh/cm$^2$ and tested under varied pressure.

The CE is a convenient way to quantify the extent of excess stripping capacity relative to the plated capacity and can be used to help understand whether dead Li or soft short circuits are contributing. CE is defined as 100% multiplied by the ratio of stripping capacity to plating capacity in any given cycle. The CE versus cycle number in Figure 2A confirms that all cells cycled at pressures above 0 MPa exhibit many cycles where the CE is higher than 100%. CE above 100% on any given cycle is not necessarily problematic or unexpected because dead Li that has become stranded in a previous cycle can reconnect in later cycles. This reconnection can result in recovered capacity that was previously lost and manifests with CE above 100% for that cycle. However, the cumulative average CE (CE$_{CA}$) must stay below 100% if dead Li is responsible for excess capacity. We define CE and CE$_{CA}$ for a given cycle formally by equations in the STAR Methods section. In short, the CE$_{CA}$ in cycle $x$ is defined as 100% multiplied by the ratio of the sum of the stripping capacities in cycles 1 to $x$ to the sum of the plating capacities in cycles 1 through $x$. If the CE$_{CA}$ is higher than 100% in any cycle, then the total capacity during all stripping steps exceeds the total capacity during all plating steps. CE$_{CA}$ above 100% in any given cycle *cannot* result from reconnection of dead Li because there is not enough loss in previous cycles to account for the excess capacity in the cycle of interest; instead, CE$_{CA}$ above 100% indicates a parasitic process, which likely results from a short circuit that carries current during plating and stripping but could in theory also be due to a parasitic reaction that occurs only during stripping.

Figure 2B confirms that the CE$_{CA}$ is higher than 100% during portions of cycling for all cells cycled with pressure and is never over 100% for cells cycled at 0 MPa. This indicates that there is parasitic capacity during stripping for all cells cycled above 0 MPa. The implication is that while pressure may help preserve Li inventory, it may also exacerbate short circuits. We note that any shorts present in these cells should be distinguished as "soft shorts" because the cells polarize to the 1 V cutoff on stripping, as shown in Figures 1A–1D. We intentionally apply a cutoff voltage of 1 V rather than a time limit that would constrain the stripping current to the expected capacity. Using a 1 V cutoff instead enables cells to continue passing current beyond the expected capacity to reveal if there is parasitic capacity associated with a short circuit and alternatively to enable stripping of dead Li that can become stranded in a given cycle but can sometimes be recovered in later cycles. We define "hard shorts" as robust electronic bridges between the working and counter electrodes caused by Li dendrites or some other feature that enables direct electronic contact such that essentially all of the current can be carried by the short. Such hard shorts manifest in the electrochemical data by the overpotential dropping to near zero during plating and stripping as well as the absence of polarization to 1 V during stripping. Because the cells in Figure 1 all polarize to 1 V, we designate potential short circuits as soft shorts to indicate capacity arises from *both* shorts and from conventional charge transfer reactions associated with plating and stripping. Soft shorts are possible if the electronic bridges are small or have

**Table 1. Approximate thicknesses of deposits from cross-sectional images after one deposition at 4 mA/cm² to 2 mAh/cm² at varied pressure**

| Pressure (MPa) | Thickness of deposit 4 mA/cm² (µm) | Thickness of deposit 0.5 mA/cm² (µm) |
|---|---|---|
| 0 | 44 | 91 |
| 0.01 | 22 | 33 |
| 0.1 | 21 | 30 |
| 1 | 19 | 22 |

All thicknesses were measured on working electrodes extracted from Li versus Cu pouch cells with two Celgard 2325 separators after one Li deposition step on the initially pristine Cu working electrode to 2 mAh/cm² with varied pressure. Thicknesses were corrected to account for the angle of the cross-sections (52°). The thickness of the Li deposited at 0 MPa is measured from the image in Figure 3. However, it is not representative of the thickness for the entire sample, as is demonstrated in Figure S10. Thicknesses collected herein at 4 mA/cm² are compared to those previously reported for cells cycled at 0.5 mA/cm² and are reprinted with permission from Harrison et al., ACS Applied Materials & Interfaces, 13, 31,668-31,679. Copyright 2021 American Chemical Society. A comparison of the images at 4 mA/cm² with additional images corresponding to the same samples previously published at 0.5 mA/cm² are presented in Figure S9.

significant resistance such that they cannot carry all of the programmed current or are destroyed by carrying the current.

### Cryo cross-sectioning and imaging of Li morphology

To understand how the parasitic stripping capacity (and higher than 100% CE$_{CA}$) is related to soft short circuits, we start by performing ex-situ imaging characterization to better understand morphology after one Li deposition on the copper working electrode. Our previous work reveals that applied pressure significantly densified Li plating morphology at a low current density of 0.5 mA/cm², such that deposits at 0 MPa were 5x thicker than deposits at 1 MPa (Harrison et al., 2021). These previously determined thickness values are summarized in Table 1. Figure S9 provides cross-sectional images similar to those in our previous work at low current density for convenience to compare directly to the high current density images shown herein. Although the largest thickness changes are observed between the 0 and 0.01 MPa pressures, there are significant decreases in thickness with each increase in pressure for cells cycled at 0.5 mA/cm².

Deposits from cells cycled at 4 mA/cm² also exhibit a large decrease in thickness when increasing the pressure from 0 to 0.01 MPa (Figure 3, Table 1). However, Figure 3 is a little misleading because the thickness of deposits varies drastically for cells cycled at 0 MPa. Figure S10 shows a photograph and a low magnification cryo SEM image that evidence the non-uniform Li deposition in cells cycled at 0 MPa. Therefore, it is difficult to select one reasonable region for cryo FIB and the thickness of the deposit at 0 MPa in Figure 3 is not representative of the entire sample. We suspect that the non-uniform deposition stems from pouch cells having floppy packaging that can enable differences in the gap spacing and waviness across the electrode stack unless at least a small amount of pressure is applied to push the electrodes together with a reasonably uniform spacing. We observed a drop in series resistance with increasing pressure between 0 and 1 MPa in our previous work, with the largest drop occurring between 0 and 0.01 MPa, suggesting the gap spacing between electrodes shrinks with pressure (Harrison et al., 2021). Non-uniformities in gap spacing and, therefore, ion transport distances, between electrodes are expected to be especially important at high current density where transport is limited, so gap spacing non-uniformity is expected to cause non-uniformities in plating and stripping, as is observed in Figure S10. Because deposits from the 0 MPa cells exhibit non-uniform thickness across the sample and we suspect the image at 0 MPa is not representative of the entire sample, we will focus on comparing images from samples cycled at 0.01–1 MPa, where the deposition is more uniform.

Like the cells cycled at 0.5 mA/cm², the cells cycled at 4 mA/cm² with 0.01–1 MPa of pressure show a decrease in thickness with increasing pressure. However, the changes in thickness with pressure are much smaller in cells cycled at 4 mA/cm² than those in cells cycled at 0.5 mA/cm²; cycling at 4 mA/cm² results in consistently thinner deposits relative to cycling at 0.5 mA/cm² (Table 1), except at a pressure of 1 MPa, where the thickness is similar between the two current densities (though still slightly lower at higher currents). These results could be considered surprising because one might expect the opposite, that high aspect ratio dendritic structures typically associated with high current density cycling would exhibit less
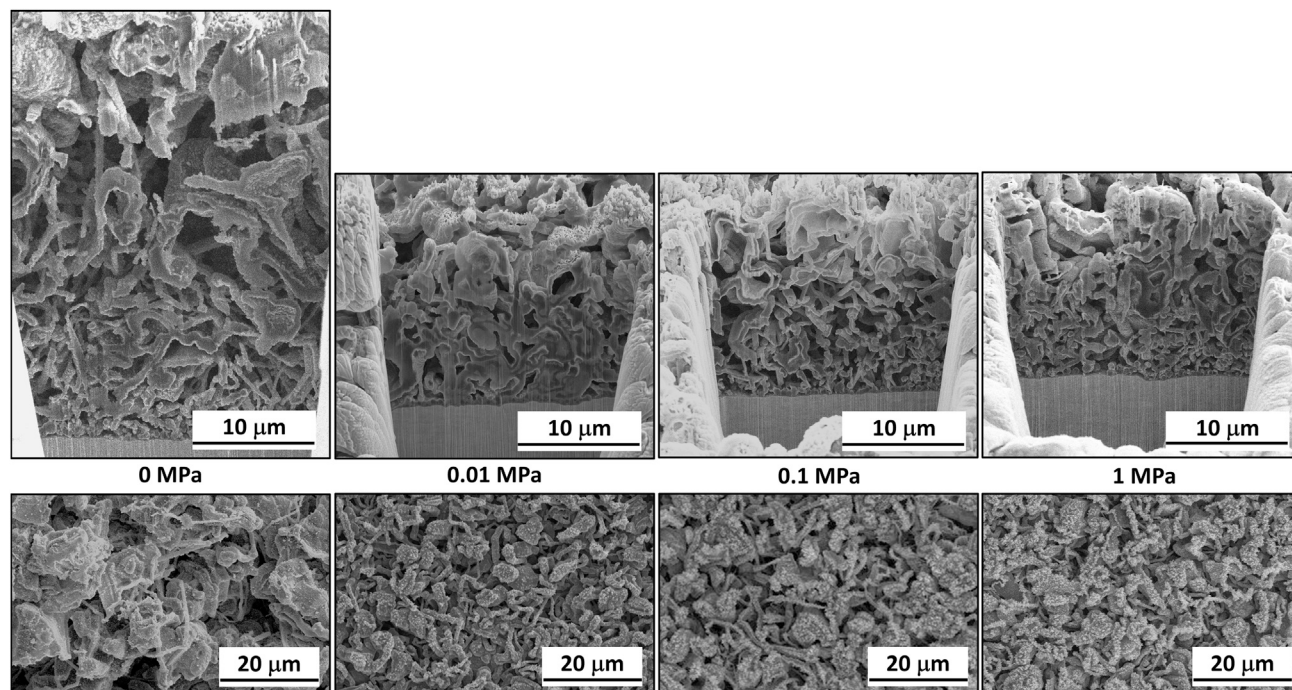
**Figure 3. Scanning electron microscopy images showing lithium morpology after one deposition step at various applied pressures**

Ex-situ cross-sectional cryo SEM images (top row) and plan view images after cryo Ga$^+$ FIB milling (bottom row) of working electrode samples extracted from Li versus Cu pouch cells with two Celgard 2325 separators. Images are taken after Li was electrodeposited one time on pristine Cu working electrodes at 4 mA/cm$^2$ to 2 mAh/cm$^2$ with varied pressure. The image shown for the 0 MPa sample is likely not representative of the entire sample because the thickness varies significantly with location, as is shown in Figure S10. Scale bars are all 10 μm for the top row and 20 μm for the bottom row of images.

compact morphologies than at low current density. Instead, the low current density deposits are always thicker than those at high current density. Also surprising is that thickness changes significantly with pressure at low current density but pressure impacts thickness more mildly at high current density (between 0.01 and 1 MPa).

We attribute the compact and relatively pressure-insensitive deposit morphologies in cells tested at high current density at pressures ranging from 0.01 to 1 MPa to overpotential differences between low and high current densities. At low current, Li$^+$ ions can transport relatively easily because they are produced and consumed at a lower rate by electrochemical reactions (Harrison et al., 2021). Therefore, the Li$^+$ ions can transport longer distances to nucleate and grow at the most favorable sites, provided by defects for example. The expected low nucleation density at low current relative to high current has been documented in the literature (Sanchez et al., 2020; Pei et al., 2017; Biswal et al., 2019) and is corroborated by comparing the deposit morphology in Figure S9, where the size of deposits at 0.5 mA/cm$^2$ are much larger than those at 4 mA/cm$^2$. The larger deposits at low current density are consistent with lower nucleation density, which is expected to lead to fewer deposits, so each deposit grows more extensively. At low current, in the absence of pressure, deposits are free to grow into very porous and thick structures. Generally, the overpotential is small at low current density, but there is a mechanical overpotential that becomes increasingly important at higher pressures. Growing Li deposits must perform work to displace the pressurized interface, so there is an incentive for more compact deposits to form at higher pressure because less work is required if the Li deposits in a dense morphology, which corresponds to minimal interfacial displacement (Zhang et al., 2019). Because the other overpotentials are small at low current densities, the mechanical overpotential can be significant at high pressure and can greatly impact the nucleation and growth process as well as the resulting morphology. At high pressure, the overpotential related to transport limitations is significant and Li$^+$ ions cannot easily redistribute to nucleate and grow only at favorable sites because the Li$^+$ ions are depleted quickly to accommodate the reaction rates required at high current densities and do not have time to transport to only the most favorable nucleation sites. Therefore, nucleation and growth are more uniform at a high current density and denser deposits are favored because Li$^+$ ions combine with

electrons to form Li metal wherever they can keep up with transport. At high current density, the overpotential related to transport is much larger than at low current and the morphology is already more uniform, so the mechanical overpotential plays a much less significant role in controlling morphology at high current than at low current.

Because Li metal is known to be susceptible to creep (Zhang et al., 2020) when force is applied, we expect that creep also may play a role in the observed Li morphological evolution shown here. Creep should promote denser deposits and is increasingly significant at longer times and higher pressures. Depositing 2 mAh/cm$^2$ of Li electrochemically requires 4 h at 0.5 mA/cm$^2$ but only 30 min at 4 mA/cm$^2$, so we expect creep to be more significant at low current densities because there is more time for it to densify deposits. Therefore, the large changes in thickness observed at low current density are consistent with increasing effects of creep in samples deposited with increasing pressure. The decreased sensitivity of deposit thickness to pressure at high current density may be partly explained by creep not having as much time to densify the samples; however, creep cannot alone explain the observed morphology. If creep was the only contributor to deposit density, one would expect the low current density deposits to always be denser than those at high current density due to longer time under pressure. In contrast, at 1 MPa, where we expect creep to play the most significant role in densifying morphology, the high current density deposit, which is under pressure for 8x less time, is actually *denser* than the deposit at low current density. Therefore, while we expect that creep, nucleation, and the overpotential differences discussed in the previous paragraph all contribute to changes in deposit morphology at low and high current densities, we believe the overpotential effects and nucleation differences impact the morphology most significantly. Understanding this complex relationship between current density, morphology, and mechanics more thoroughly will be the subject of future work.

We observe no obvious vertically oriented dendrites or needle-like structures during cell disassembly or in Figure 3 for cells cycled at 4 mA/cm$^2$ that appear positioned to likely pierce the separator and cause a short circuit following one Li deposition at any pressure. However, the images do show high aspect ratio deposits with wiry structures that are more likely to be able to cause short circuits after extended cycling than the larger deposit morphologies shown previously at low current density (Harrison et al., 2021) and in additional images shown in Figure S9. The literature demonstrates that Li mechanical properties are size-dependent and smaller structures exhibit higher yield stresses (Xu et al., 2017), so smaller structures may be more likely to pierce through separators and cause short circuits. Furthermore, smaller deposits are closer in size to nanoscale pores in separators, also enabling easier penetration. Finally, although Li is a soft metal, it is always covered with a harder SEI shell, which likely increases the overall hardness of the structure (Jungjohann et al., 2021), so the smaller, high aspect ratio deposits observed at high current density have a larger proportion of SEI to bulk Li such that they are likely to be harder overall as a composite structure and therefore more prone to piercing a separator than larger deposits after low current density cycling.

Regardless, dendrites and short circuits are more likely to form after extended cycling, so it is unsurprising that they are not obvious after only one deposition. Therefore, we attempted similar ex-situ cryo Ga$^+$ FIB and SEM after the 51$^{st}$ Li deposition step. However, cell disassembly was often difficult because the deposits were difficult to remove from the separator. This disassembly difficulty is consistent with dendrites growing into the separator, so it would be ideal to cross-section and image the entire electrode stack because disassembly would involve ripping apart the interfaces for these particular samples. Conventional cryo Ga$^+$ FIB milling rates are too slow to allow milling through entire electrode stacks or even milling through the separator down to the working electrode in reasonable times. In order to perform ex-situ cryo Ga$^+$ FIB and SEM, the separator must be removed, which potentially destroys the dendrites we are trying to identify. Hence, we employ a cryo laser PFIB to athermally mill through electrode stack cross-sections while preserving the interfaces of interest within the electrode stack, as we have previously demonstrated for coin cells (Jungjohann et al., 2021). We first attempted using the laser PFIB technique with pouch cells on the cryo stage, but it proved difficult to keep entire large pouch cells frozen on a small cryo stage. Therefore, herein we disassemble pouch cells, carefully cut sections out of the electrode stacks with nonconductive ceramic scissors, and rebuild the cut-out sections into coin cells to enable protected environment transfer of assembled electrode stacks to the laser cryo PFIB/SEM. We freeze the coin cells on a cryo stage and use the laser PFIB/SEM to mill through the coin cells and image the electrode stacks in cross-section. This process to extract pouch cell stacks and rebuild them into coin cells for cryo laser PFIB milling and cryo SEM imaging is described by the cartoon in Figure 4A.
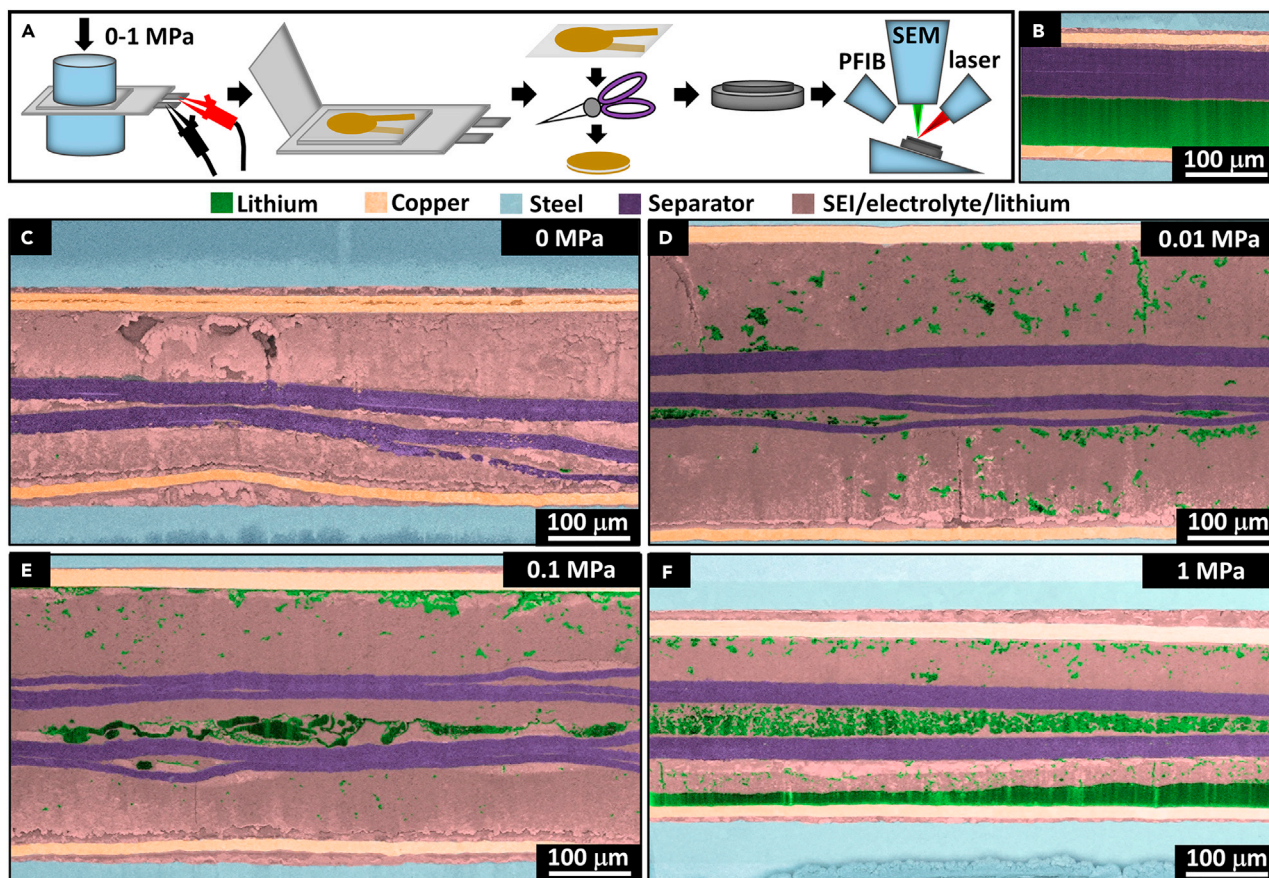
**Figure 4. Scanning electron microscopy images after 51 lithium deposition and 50 stripping steps**

Cryo SEM images after cryo laser PFIB milling of stacks cut out from pouch cells following the procedure depicted in (A) for Li versus Cu pouch cells cycled at 4 mA/cm$^2$ to 2 mAh/cm$^2$ with pressures of (C) 0 MPa, (D) 0.01 MPa, (E) 0.1 MPa, and (F) 1 MPa. Images are artificially colored for easier interpretation. The image in (B) depicts a pristine fabricated coin cell that is uncycled without having been previously fabricated or cut out of a pouch cell. This pristine coin cell is prepared similarly to the pouch cells except the working electrode Cu current collector is 9 μm thick rather than 20 μm thick. It is provided as an example before cycling to help with interpretation of the other figures. The schematic in (A) depicts the procedure to prepare pouch cell samples for cryo laser PFIB milling and cryo SEM imaging. Cells are first cycled in pouch cells with varied pressure and then they are disassembled such that stacks are removed. A section of each stack is then extracted carefully with insulating, ceramic scissors in sizes appropriate for coin cells. Then the stack sections are rebuilt into coin cells with no additional cycling before laser PFIB milling and cryo SEM imaging. Some of the lighter contrast regions within the SEI/electrolyte/Li areas are likely due to redeposition of steel from the milling process. The image shown for the 0 MPa sample is likely not representative of the entire sample because the thickness varied significantly with location, as is shown in Figure S20. Scale bars are all 100 μm.

Cryo SEM images of electrode stacks after cryo laser PFIB milling are also shown in Figure 4. These electrode stacks are removed from pouch cells after being cycled 50$^1/_2$ times (51 Li deposition and 50 stripping steps) at pressures of 0, 0.01, 0.1, and 1 MPa. The images are artificially colored to enable easier image interpretation, as informed by previous work examining how Li appears through contrast, surface texture, and energy dispersive spectroscopy maps (Jungjohann et al., 2021). For clarity, raw images corresponding to all colored images are presented in Figures S11–S19. A pristine, uncycled cell is shown in Figure 4B with the 50 μm Li (colored green) on Cu (colored peach) laminate counter electrode on the bottom of the image, the Cu (colored peach) working electrode on the top, and with two Celgard 2325 separator sheets (colored purple) between the electrodes. Using two separator sheets is common in laboratory scale cell fabrication (Liao and Ye, 2018; Albertus and Newman, 2008; Schweikert et al., 2012). Each sheet of Celgard 2325 is comprised of trilayers including two layers of polypropylene on either side of a layer of polyethylene. The pristine Li metal before cycling displays a distinct textured pattern, which is laser-induced, and enables easy detection of pristine, uncycled Li. We have previously demonstrated that this pattern is unique to bulk Li by comparison to control experiments on pristine cells and by looking for voids in energy dispersive spectroscopy maps, which indicate Li metal (Jungjohann et al., 2021).

**Table 2. Thicknesses of deposits shown from cross-sectional images after 50 $^1/_2$ cycles at 4 mA/cm$^2$ to 2 mAh/cm$^2$ at varied pressure**

| Pressure (MPa) | Thickness working electrode (μm) | Thickness counter electrode (μm) | Thickness electrodes and separator (μm) |
|---|---|---|---|
| 0 | 84 | 35 | 189 |
| 0.01 | 120 | 110 | 318 |
| 0.1 | 90 | 73 | 274 |
| 1 | 52 | 52 | 188 |

Cells consist of electrode stacks extracted from Li versus Cu pouch cells with two Celgard 2325 separators, cut with ceramic scissors into smaller diameter stacks, and rebuilt into coin cells for imaging. Thicknesses were corrected to account for the angle of the cross-sections (59-60°). These values vary across the cells and are intended to signify approximate nominal values. Thicknesses of electrodes include the Li, separators, and SEI/electrolyte/Li layers in Figure 4 without the Cu current collector layers included. The thickness of the Li deposited at 0 MPa is measured from the image in Figure 4. However, it is not representative of the thickness for the entire sample, as is demonstrated in Figure S20.

Cells cycled at varied pressure 50$^1/_2$ times are shown in Figures 4C–4F. A pristine, uncycled bulk Li reservoir (colored green) is present at the counter electrode only in the cell cycled at 1 MPa, indicating that the initial excess Li reservoir has not been depleted in cells cycled at 1 MPa. In contrast, the counter electrodes of cells cycled at lower pressures exhibit only porous SEI and electrolyte (colored pink) at the current collector interface, which is likely decorated with small domains of dead or delicately connected Li (only the largest of which is easily detected and colored green). These observations are consistent with the electrochemical data shown in Figure 1, where only the cells cycled at 1 MPa can cycle 50 times without capacity loss. Therefore, the cryo laser PFIB/SEM images confirm that the pristine Li reservoir at the counter electrode is better preserved at 1 MPa than at the other pressures, which provides additional evidence that the diminishing plating and stripping capacities in late cycles at pressures of 0, 0.01, and 0.1 MPa result from loss of the pristine excess Li reservoir at the counter electrode.

The images in Figure 4 also reveal that, although the deposits after one Li deposition exhibit no significant decrease in thickness with increased pressure from 0.01 to 1 MPa, increasing pressure enables much denser electrode stacks after 50 $^1/_2$ cycles in the same range of 0.01–1 MPa. Table 2 shows measurements of the working electrode, counter electrode, and total stack thicknesses at each pressure. More compact Li deposits at higher pressure are desirable because thinner deposits resulting from the same cycled capacity enable increased practical volumetric energy density. The thickness of the electrode stack cycled without pressure does not follow the trend of the three pressurized cells where the thickness of the stack decreases with increasing pressure. However, as discussed in reference to ex-situ imaging in Figures 3 and S10 after one deposition, there is a lot of variation in thickness for cells with Li deposited at 0 MPa and deposition is highly non-uniform. We tested multiple samples and locations in cells cycled at 0 MPa, and Figure S20 confirms that there is significant variation in the thickness with location. It is clear from the additional images that the separator and electrodes tend to be less aligned horizontally. In contrast, cells cycled at higher pressures show that the Cu and separator layers are reasonably aligned with the horizontal plane. The 0 MPa stack image in Figure 4C exhibits significantly sloping separator layers and the Cu counter electrode is bowed with what is likely electrolyte or SEI/Li between the Cu current collector and the steel spacer below it. These observations are common in 0 MPa cells, as shown in Figure S20, indicating that deposition is not as uniform at 0 MPa as in cells even with a small amount of pressure. The variation in thickness and sloping and the wavy nature of the stack with location at 0 MPa likely stems from the fact that pouch cells do not have a rigid case. Therefore, in the absence of any applied pressure, the distance between the electrodes varies with slight variations in thickness or waviness of the thin and floppy pouch casing. In contrast, with even slight pressure (0.01 MPa), the electrode stack is much more likely to adopt a relatively uniform thickness throughout because the case is forced to conform to the gap between the platens.

The thick deposits on the Cu working electrode current collectors after cycling shown in Figures 4C–4F differ significantly from the 50 μm layer of pristine, uncycled Li metal shown in Figure 4B, which are all depicted at the same scale. The images predominantly show a sea of other material (colored pink) where we would expect Li metal, but this other material is not recognizable as bulk Li. We discount that the material is simply electrolyte (which is frozen under cryo conditions) because the pressure in these cells should enable a reasonably compressed and compact electrode-electrolyte interface where electrolyte would be pressed

out to the edges of the cell. Only a small amount of electrolyte is expected to fill gaps that arise due to interfacial roughness. Instead, we believe that the material is porous SEI, likely mixed with small domains of Li and frozen electrolyte filling the gaps between SEI and Li domains. Porous Li and SEI structures are expected based on the morphology shown in Figure 3. The texture of the SEI/electrolyte/Li regions may result from these regions being porous mixtures, where a scaffold of SEI intermixed with small domains of Li is infiltrated by electrolyte in the pores. The texture of the images in these mixed regions may provide information about the pore sizes or may simply result from unique laser material interactions. We note that we observe more texture at lower pressure, where we also expect more porosity, according to Figure 3, supporting the idea that the texture may be linked to the porous structure. While the laser PFIB milling process has the advantage of enabling intact coin cells to be cross-sectioned in minutes, it does not allow the samples to be washed, as they can be prior to cryo Ga$^+$ FIB milling. Therefore, the electrolyte remains in place and can be difficult to distinguish from SEI and Li. These pink colored regions also exhibit some lighter contrast areas, which are likely the result of redeposition of steel during the milling process. The redeposition is not fully cleaned from the sample during polishing steps if the steel deposits in large gaps or cracks on the cut face.

There are a few regions (colored green) within the sea of material colored pink where Li is present in large enough domains to be obvious. Domains of Li that are smaller than the laser wavelength would not interact to produce the laser-induced pattern we observe in pristine, uncycled Li so small domains likely covered in SEI are much more difficult to identify. Evidence for nanometric domains of disconnected or weakly connected Li in a sea of SEI has been demonstrated previously through cryo transmission electron microscopy experiments (Fang et al., 2019). Because these cells can all still cycle after 50.5 cycles (evidenced by finite capacity in Figure 1), there is some accessible Li remaining in the cell, but it is likely to be present in small domains that are electrodeposited from previous cycles rather than as bulk Li remaining from the initial counter electrode excess. However, it is clear that a significant amount of Li inventory is lost to SEI and small domains of Li, some of which are likely dead or easily can become dead with continued cycling, and there is large cell expansion due to the SEI reaction. Because the electrodes are significantly thinner in general at higher pressure (with the exception of 0 MPa that varies with location), the losses of Li inventory to SEI and dead Li domains appear at first glance to be more significant at lower pressure than at higher pressure and cycling appears to be more efficient at higher pressure in terms of Li inventory preservation.

Perhaps more significantly and surprisingly, the cryo laser PFIB/SEM images reveal varying degrees of material accumulating between the separator sheets. Additionally, some images also show that the trilayers in each separator delaminate (particularly at low pressure) and material accumulates between the trilayers. We have previously documented even more severe separator damage in cells cycled at 1.9 mA/cm$^2$, with a lower concentration LiFSI DME electrolyte in coin cells without pressure variation (Jungjohann et al., 2021), so this separator damage is consistent with previous results. The accumulated material likely arises from Li and SEI growing through the separator. It is also possible that disconnected bits of dead Li and SEI are pushed through the separator through pores, but that is unlikely due to the tortuous path that would be required and the large, continuous deposits of bulk Li evident between separators in some of the images. At low pressures of 0 MPa, there is very little evidence of bulk Li domains (colored green) between the separators in Figure 4C, but a location with a small Li deposit is shown in Figure 5A at a higher magnification. At 0.01 MPa, Li metal deposits are not widely prevalent between the separators, although there are several clear Li deposits (colored green) between trilayers near the counter electrode, which are shown in Figures 4D and 5B. It is worth noting that other small Li metal deposits may exist but may be covered with SEI and be too small to detect easily and distinguish from SEI and electrolyte at this magnification. It is likely that there was once or still is active Li in locations where material has accumulated between separators because a conductive path is needed to grow SEI and deposit Li between the separators. In fact, the presence of Li and SEI in the separator further suggests that small Li metal domains are present throughout the regions colored pink and that interconnected Li domains enable electron transfer throughout these regions to support electrochemical reactions far from the current collector and continuous growth of Li and SEI within the separator.

At higher pressures of 0.1 and 1 MPa, Li metal deposits present between the separator sheets are very obvious, as shown in Figures 4E, 4F, 5C, and 5D. However, at 0.1 MPa, the large Li deposits span horizontally and do not appear to continuously connect the top and bottom separator sheets, at least on a bulk scale. They are also more distributed closer to the counter electrode than the working electrode, which may
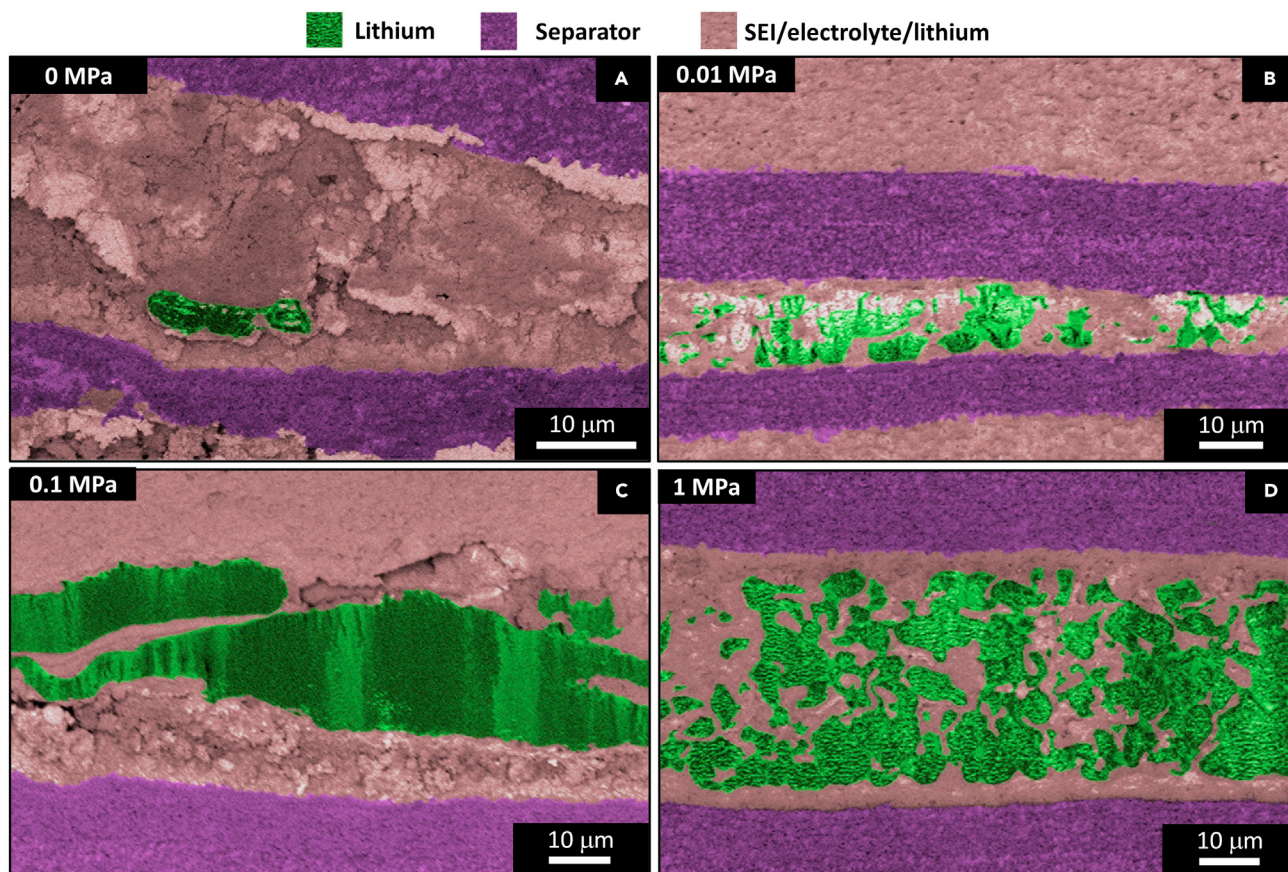
Lithium | Separator | SEI/electrolyte/lithium

**Figure 5. Magnified scanning electron microscopy images after 51 lithium deposition and 50 stripping steps**

Cryo SEM images after cryo laser PFIB milling of stacks cut out from pouch cells following the procedure depicted in Figure 4A for Li versus Cu pouch cells cycled at 4 mA/cm² to 2 mAh/cm² with pressures of (A) 0 MPa, (B) 0.01 MPa, (C) 0.1 MPa, and (D) 1 MPa. These are the same samples as in Figure 4 but with higher magnification to highlight the locations between layers of each separator or between sheets of the two separators which show Li metal plating. Some of the lighter contrast regions within the SEI/electrolyte/Li areas are likely due to redeposition of steel from the milling process, particularly in (A). Scale bars are all 10 μm.

provide insight into their origin. At 1 MPa, the deposits form nearly a continuous layer of Li spanning between the two separator sheets, as is most obvious from the magnified image in Figure 5D. The increasing amount of obvious Li between the separators and more continuous paths of the Li deposits at higher pressures indicate that pressure exacerbates the likelihood of soft short circuits. We note that we did not have to cross-section these cells in multiple areas and search to find evidence of Li and SEI in the separators, but rather this evidence was present in the first randomly selected locations we examined. This suggests that, rather than a single distinct dendrite that pierces the separator and causes a hard short, the Li penetration and redirection between separators that likely evidences short circuits appears to be widespread and occur over significant areas with many entry points rather than at a single location caused by a local imperfection such as a defect for example.

We image these samples after cycling 50½ times with the goals of understanding how pressure impacts the Li inventory retention at the counter electrode and to understand whether evidence of dendrite growth or short circuits could be observed. While it would have also been informative to image cells in the early cycling range of 5–15 cycles, where many cells show evidence of parasitic capacity (higher than 100% $CE_{CA}$), this would not have achieved the goal of understanding the Li inventory retention. However, we suspect that the SEI/Li penetration into the separator is a gradual process with cycling based on imaging the evolution of SEI/Li accumulation and penetration into the separator with cycling in previous work (Jungjohann et al., 2021). Our previous work focused on coin cells without pressure variation and with a lower concentration but similar electrolyte and lower current density, so it is not exactly analogous. However, therein,

we observed evidence of SEI/Li growing into the separator even as early as after the first deposition, and the SEI/Li growth generally increased with increasing cycle number, eventually leading to destruction of the separator. Therefore, we expect that imaging after earlier cycles would provide similar evidence of gradual SEI/Li growth into the separator with increasing cycling, but we have not performed that analysis herein.

The laser PFIB/SEM images in Figures 4 and 5 reveal Li metal growing into the separators and accumulating/redirecting between the separator sheets, which has several important implications. First, Li growth into the separators strongly suggests that there are short circuits in these cells, as is already suspected from the electrochemical data. The CE data suggests that these soft shorts form very early in cycling and potentially become disconnected later when the CE drops below 100% again. Future work will focus on identifying the onset of Li plating within the separators. Second, it is possible that the cell cycled at 1 MPa only exhibits improved Li inventory retention and thinner deposits because soft short circuits are more severe, which could improve efficiency if a more significant amount of current is carried through the short, such that a smaller portion of the current is carried by charge transfer reactions. Therefore, though the electrochemical data suggests that cycling may be more efficient and Li inventory may be better preserved at high pressure, this may just be an artifact of the higher propensity to form short circuits at high pressure. It has been previously suggested that Li growth though the separator in Li symmetric cells may lead to the appearance of stable cycling if the short circuits never transition to hard shorts (Albertus et al., 2018). Third, the identification of short circuits and accumulation of Li between the separators is uniquely enabled by the cryo laser PFIB/SEM approach that allows imaging of large areas of electrode stacks without cell disassembly, and the growth of Li into the separator would not have been detected with conventional cryo $Ga^+$ FIB and SEM imaging (where the separator would have been removed completely and not imaged). The thicknesses of ex-situ electrode deposits would not have accurately depicted the total thickness of deposits (or the resulting practical volumetric energy density) because there are significant amounts of SEI and Li between the separators. Fourth, if only one separator sheet had been used rather than two sheets, these cells would likely have shorted. This implies that the use of two separators can be considered a way to delay catastrophic short circuits. Use of two separator sheets has also been shown to improve performance relative to only one in Li/S batteries (Liao and Ye, 2018), has been previously touted to likely delay the onset of Li dendrite penetration (Albertus and Newman, 2008), and has been shown to increase cycle life of Li anodes with increasing numbers of separator sheets (Kanamori et al., 2020). Alternatively, instead of a mitigation to improve performance, the use of multiple separators could be seen as a crutch that makes short circuits more difficult to detect because the Li can redirect between the separator sheets rather than revealing that the cell is failing.

### Effects of one versus two separator sheets

To confirm that use of two separator sheets delays obvious detection of soft short circuits by enabling Li to redirect between the separator sheets, we fabricate pouch cells with only one Celgard 2325 separator and we cycle the cells 50 $\frac{1}{2}$ times. Voltage versus time and capacity versus cycle number plots are provided in Figure 6 for pouch cells fabricated with only one separator. The cells cycled at 0 MPa with one separator, shown in Figures 6A and 6E, perform similarly to those cycled with two separators, shown in Figures 1A and 1E. Figure 7 also confirms that CE and $CE_{CA}$ of cells cycled at 0 MPa with one separator are similar to those cycled with two separators (Figure 2). In short, electrochemical signatures for cells at 0 MPa do not show any obvious signs of short circuits regardless of the number of separators. In contrast, the cells cycled with 0.01, 0.1, and 1 MPa of pressure exhibit more obvious soft short circuits with one separator, indicated by sudden and significant drops in overpotential to nearly zero in Figures 6B–6D and 6F–6H and $CE_{CA}$ above 100% in Figure 7. We cycle several replicates of each condition and select a representative replicate for presentation in Figures 6 and 7, but we present the replicates in Figures S21–S24 to show that the differences in behavior with one and two separators are obvious in many replicate cells. In fact, we find that some cells cycled at 0.01 and 0.1 MPa with one separator exhibit even more obvious shorts than the cells selected for Figure 6. All cells cycled at 1 MPa exhibit similar obvious and severe soft short circuits and all cells cycled at 0 MPa exhibit no evidence of soft short circuits. The result that use of only one separator leads to more obvious short circuits in cells cycled under pressure is consistent with the imaging results in Figure 4 that show Li deposits readily penetrating the separator and redirecting between the two separator sheets. Had there only been one separator in each of those cells, the cells would have shorted more obviously. Therefore, we confirm our assertion that two separator sheets reduce the severity of soft short circuits by
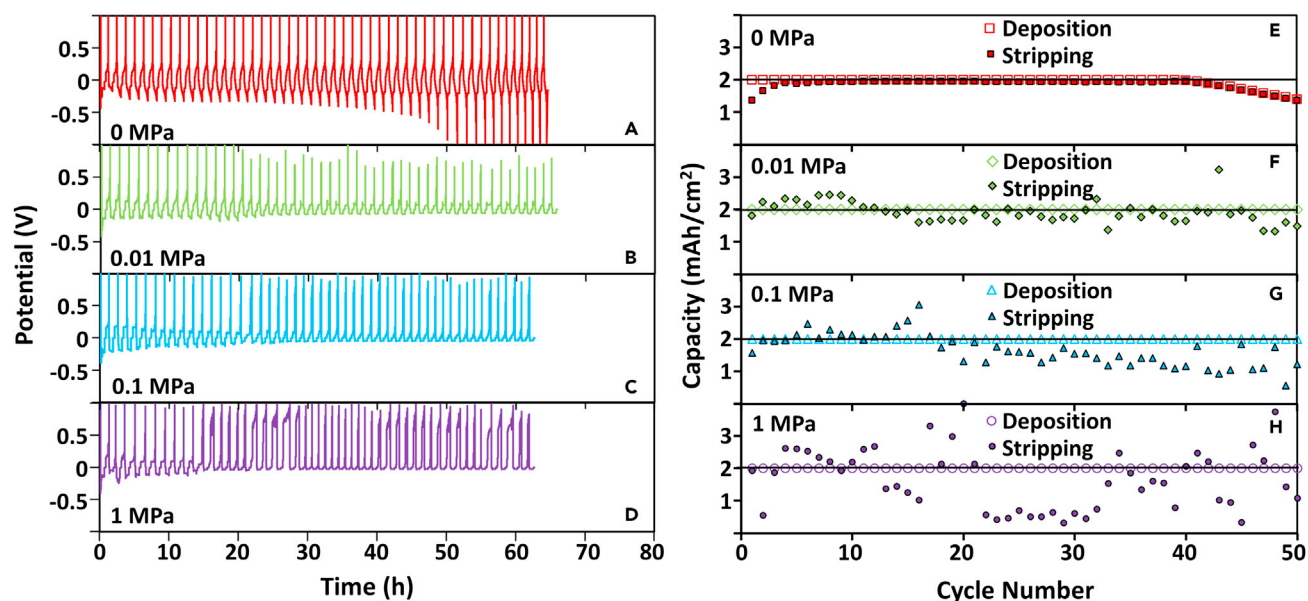
**Figure 6. Electrochemical data for cells cycled at various applied pressures with one separator sheet**
Potential versus time (left) and capacity versus cycle number (right) data for Li versus Cu pouch cells with only one sheet of Celgard 2325 separator (as opposed to two sheets in Figure 1) cycled at 4 mA/cm$^2$ to 2 mAh/cm$^2$ and tested under 0 MPa (A and E), 0.01 MPa (B and F), 0.1 MPa (C and G), and 1 MPa (D and H) of pressure.

redirecting them between the separators. However, it is important to note that this likely is not an effective mitigation and likely masks or delays rather than solves the problem of Li growing through the separator.

To corroborate that soft short circuits are masked but likely are still prevalent in cells with two separators, we present electrochemical impedance spectroscopy (EIS) data in Figure 8 after 1, 5, and 51 Li depositions on the working electrodes and compare cells with one and two separators. After one Li deposition, cells cycled with one separator generally exhibit a slightly lower solution resistance compared to cells with two separator sheets, which is expected because the gap spacing decreases by half in cells with only one separator, so there is a shorter transport distance. The solution resistance also decreases with increasing pressure after one deposition, suggesting that pressure shrinks the gap spacing between electrodes, as we have observed previously as well (Harrison et al., 2021). Semicircles arising due to interfacial reactions are very similar with one or two separator sheets after one deposition, indicating that the deposition process is similar in either case. It is common to observe multiple semicircles because they can correlate to reactions at interfaces on the two different electrodes or to different Li environments (i.e., pristine versus electrodeposited Li). There are subtle changes with pressure after one deposition, but the changes between pressures are consistent with one or two separator sheets.

Deposition 5 was chosen as an intermediate cycle number because all of the cells cycled with pressure exhibit higher than 100% CE$_{CA}$ after the fifth deposition and therefore soft shorts are likely in this cycle. The 0 MPa data exhibit two small semicircles after both depositions 1 and 5 but the cells cycled with 0.01, 0.1, and 1 MPa of pressure exhibit significant changes between the first and fifth deposition. The distinct lower frequency semicircle obvious in all cells after one deposition appears to diminish greatly after 5 depositions, although it is possible it grows and is incorporated into the low frequency tail which adopts a slightly curved shape. Semicircles shrinking in size after a few cycles have been demonstrated previously in 4 M LiFSI/DME (Qian et al., 2015; Harrison et al., 2021), even for cells cycled at lower currents where soft shorts are not likely. Therefore, shrinking semicircles in general may not necessarily indicate short circuits. However, shrinking semicircles in our cells under these conditions do appear correlated with soft shorts. Our data show the cells cycled with pressure exhibit higher than 100% CE$_{CA}$ efficiency on cycle 5, which suggests soft shorts, but cells cycled at 0 MPa show no signs of shorts in the electrochemical data (Figure 2). The behavior of the semicircles in the EIS spectra correlate well with the CE$_{CA}$ data because we observe semicircles shrinking from cycle 1 to 5 for all cells cycled with pressure, but not for cells cycled at 0 MPa.
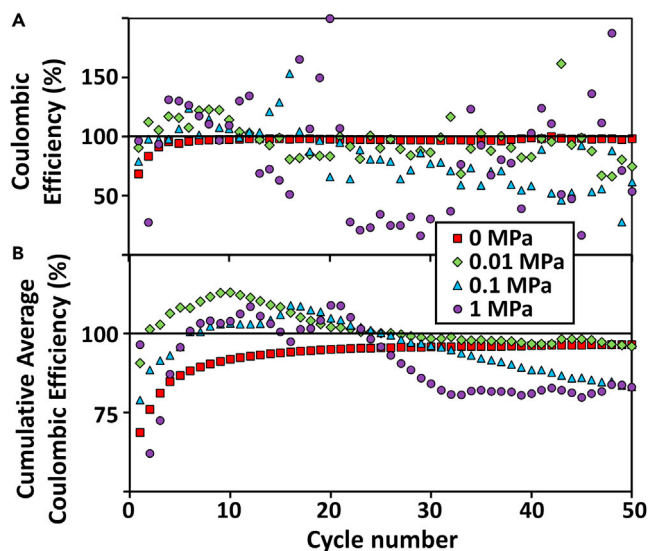
**Figure 7. Coulombic efficiency data for cells cycled at various applied pressures with one separator sheet**
Coulombic efficiency (A) and cumulative average Coulombic efficiency (B) versus cycle number data for Li versus Cu pouch cells with only one sheet of Celgard 2325 separator (as opposed to two sheets in Figure 2) cycled at 4 mA/cm$^2$ to 2 mAh/cm$^2$ and tested under varied pressure.

Furthermore, we generally observe more obvious and severe soft shorts in cells cycled with one separator sheet than two, evidenced by voltage versus time data (Figures 1 and 6), and we similarly see more severe shrinking semicircles in the EIS data when cells are cycled with one separator rather than two. These observations suggest that soft shorts are evidenced by shrinking semicircles in the EIS data under these conditions, despite previous reports at low current density that show shrinking semicircles with cycling in cells that are unlikely to experience soft shorts (Qian et al., 2015; Harrison et al., 2021).

The EIS data after 51 depositions shows no significant change between cells with one or two separators when cycled at 0 MPa but very significant changes in cells cycled at higher pressures. Cells cycled at 0 MPa are similar with one or two separators, show no signs of soft short circuits, and both conditions exhibit significant growth in semicircle size between depositions 5 and 51. The impedance growth with cycling is consistent with SEI accumulation and the loss of pristine excess Li inventory that is obvious from cycling data in Figure 1 and imaging in Figure 4. Note that the loops at low frequency evident in the 51 deposition data are likely due to insufficient rest time for the cells to relax to a stable open circuit condition before running EIS; the rest time of 5 min was sufficient in early cycles but appears to be insufficient in later cycles where the cells exhibit higher impedance. Cells with two separators cycled at 0.01 and 0.1 MPa exhibit two semicircles after 51 depositions that are larger than the semicircles after the first and fifth depositions. Like at 0 MPa, this is consistent with the cycling and imaging data which suggests loss in accessible Li inventory after extended cycling and high impedance from the accumulation of thick SEI layers. In contrast, cells with only one separator sheet cycled at 0.01 and 0.1 MPa after 51 depositions exhibit a significant drop in the solution resistance and all semicircles disappear. These observations are consistent with soft short circuits being much more obvious and prevalent in cells with only one separator sheet. Finally, cells cycled at 1 MPa with two separators still exhibit one semicircle, so the interpretation of soft short circuits is more ambiguous, similar to after 5 depositions in pressurized cells. In contrast, the cells with only one separator sheet show a drop in impedance to near zero with very little evidence of charge transfer reactions, indicating that the cells are severely shorted, which is consistent with the voltage and capacity data.

In summary, after 51 depositions, the EIS data clearly show that the cells cycled with only one separator sheet exhibit much more obvious and severe soft shorts. Also, the EIS data shows that soft short circuits are exacerbated systematically by increasing the pressure. These observations are consistent with imaging data shown in Figure 4 demonstrating that Li and SEI redirects between the separators in cells with increasing severity as the pressure increases. Therefore, because soft short circuits are more prevalent
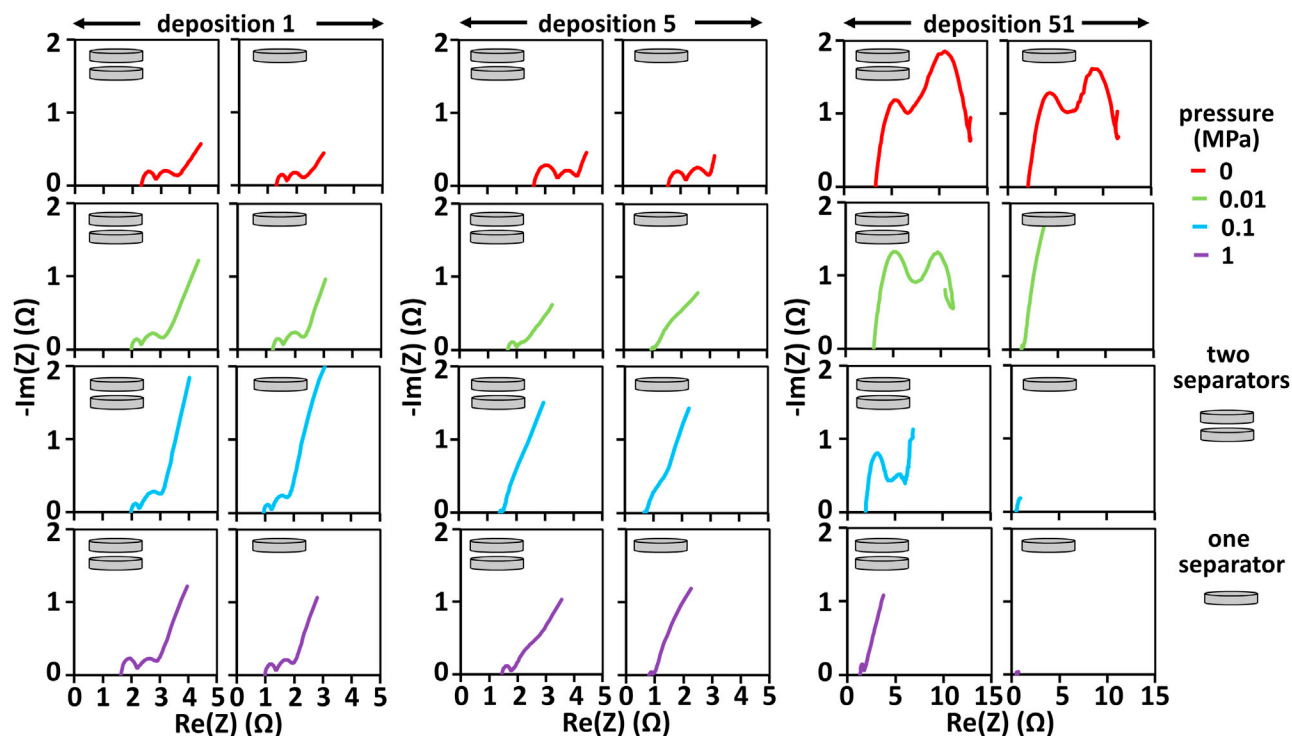
**Figure 8. Electrochemical impedance spectroscopy data for cells cycled to various applied pressures**

Electrochemical impedance spectroscopy data for cells cycled at 0, 0.01, 0.1, and 1 MPa after one (left two columns), five (middle two columns), and fifty-one (right two columns) Li depositions on Cu working electrodes in Li versus Cu pouch cells with one or two sheets of Celgard 2325 separators (as shown with cartoons) cycled at 4 mA/cm$^2$ to 2 mAh/cm$^2$.

at increased pressure, improved Li inventory retention and decreased thickness of the deposits at 1 MPa likely arise at least partly from a greater amount of the current being carried by the soft short circuits rather than completely from increased Li cycling efficiency. Utilizing less Li electrochemically with each cycle contributes to a slower loss in pristine bulk Li excess from the counter electrode.

## DISCUSSION

Herein, we present the effects of applied pressure on Li metal anode cycling at a high current of 4 mA/cm$^2$ to a capacity of 2 mAh/cm$^2$ in 4 M LiFSI in DME electrolyte. We cycle cells at 0, 0.01, 0.1, 1 and 10 MPa, but cells cycled at 10 MPa are unable to support the high current due to transport limitations and polarize to the voltage cutoff immediately. We were motivated to perform this study because we hypothesized that increased pressure may suppress dendrites that are known to cause short circuits in cells cycled at high current density. Indeed, we find that only cells tested at 1 MPa can cycle 50 times to the programmed capacity in cells fabricated with 50 μm Li counter electrodes. In contrast, cells cycled at lower pressures exhibit diminishing capacity after about 40–45 cycles. This result appears at first to suggest that pressure promotes more efficient cycling that preserves Li inventory. However, only cells tested at 0 MPa cycle reliably with no signs of soft short circuits in the electrochemical data. In contrast, cells cycled at 0.01, 0.1, and 1 MPa all show regions of CE above 100% where soft short circuits are suspect.

To better understand the electrochemical data, we cross-section and image the electrodes using a cryo Ga$^+$ focused ion beam, a cryo femto-second laser, and cryo electron microscopy techniques. Images after one Li deposition step show that pressure has little impact on morphology and thickness, except for cells cycled at 0 MPa, where the deposits are very non-uniform with location, so it is difficult to select a representative image depicting thickness. Images of entire intact electrode stacks after 50$\frac{1}{2}$ cycles reveal that (1) electrode stacks are generally more compact when cycled at higher pressure; (2) pristine, uncycled excess Li inventory remains on the counter electrode only for cells cycled at 1 MPa, which is also the only pressure that enables 50 cycles at the programmed capacity, confirming that the initial excess Li inventory on the counter electrode is consumed at all other pressures and that consumption is responsible for capacity fade; and (3) Li deposits and redirects

readily between the two separator sheets with increasing prevalence at higher pressures, suggesting that higher pressures promote soft short circuits. We also cycle cells at varied pressure with only one separator sheet and find short circuits are much more prevalent and obvious with one separator sheet rather than two, particularly when cycled at increased pressure. This indicates that the use of two separators masks soft short circuits from being easily detectable by allowing Li to redirect between separator sheets and provides further evidence that soft short circuits are *exacerbated* by increased pressure rather than *suppressed*. Consequently, we propose that high pressure preserves Li inventory and results in more compact deposits at least in part because the cells are more significantly shorted at high pressure, rather than completely resulting from more efficient cycling or morphological evolution at higher pressure. If more current is carried by soft short circuits at high pressures than at lower pressures, then less current is directly carried by the charge transfer reactions, which can then reduce Li inventory loss.

We observe significant changes in performance of Li anodes with varied pressure, which is important because laboratory cells are generally pressurized (though often the pressure is not quantified). The pressure in commercial cells varies with cell design (e.g., spirally wound, pouch, prismatic, etc.). While we have previously shown that increased pressure leads to significantly denser deposits at low current density (Harrison et al., 2021), here we show that deposit thickness is less impacted by pressure at high current density after one deposition than at low current density. Therefore, the impact of pressure on Li cycling is current density dependent. After 51 depositions, the deposit thickness on the working electrode varies significantly with pressure, but the thickness is complicated by the presence of soft short circuits after extended cycling. We show that large pressures promote short circuits, rather than suppress them, suggesting that increasing pressure is not a very effective strategy to suppress dendrites and prevent cell failure. This may be considered a benefit because high pressures may be difficult to practically apply to commercial cells, so not needing to rely on high pressure simplifies design. It is also clear that conventional separators designed for Li-ion batteries suffer from damage and Li/SEI penetration readily and likely globally throughout the cell when operating at high current density. We have shown in previous work that through-hole separator designs are even more prone to Li/SEI penetration than trilayer designs (Jungjohann et al., 2021) that we employ here. Alternative separator strategies designed to withstand high rate Li metal cycling would be a useful research direction.

### Limitations of the study

The two cryo imaging techniques used here have advantages, disadvantages, and limitations for imaging Li anodes. Ex-situ cryo $Ga^+$ FIB milling and SEM imaging of Li electrodes enables the sample to be washed of excess electrolyte before freezing so that the Li morphology can be very clearly recognized without added contributions from frozen electrolyte. This technique is well suited for probing many battery electrode materials under many conditions. However, $Ga^+$ FIB milling is slow, so the milling depth and milling area is limited, which makes it difficult to mill through entire intact electrode stacks. Because of that limitation, $Ga^+$ FIB and SEM imaging is most reasonably applied to single electrodes that are removed from the rest of the stack. Unfortunately, removing the electrode from the separator can damage the interface and destroy evidence of dendrites that may be growing into the separator in some cells, such as those cycled under the conditions in this study.

The cryo laser PFIB milling technique also used in this study has the advantage of very fast milling rates that can be used to cross-section entire cells including steel casing in mm wide areas without heating the cell. However, because the electrodes are not removed and washed, the electrolyte is frozen in place and can be difficult to distinguish from the SEI. This can also make it more difficult to recognize small Li grains. Also, though much larger areas can be imaged with the laser PFIB, it is still a relatively small part of the overall electrode and it remains time consuming to sample many cells and locations. Therefore, if the sample is not very homogeneous, this technique could lead to misinterpretation of the morphology.

Finally, the laser PFIB milling technique leads to metal debris that can be redeposited during milling onto the electrode stack. Because the electrolyte is frozen, it acts as a barrier to release of energy between potentially shorted electrodes. Herein, we have studied Li versus Cu cells, so the cells do not have a cathode with energy to release in the event of a short from metal redeposition even if the process were performed at room temperature. Therefore, there are no safety concerns in terms of heat release when the cell is brought back up to room temperature to remove from the SEM. However, if a cell with an anode and cathode were shorted during milling from redeposition of milled metal, there would be potential for energy release when the cell was brought back to room temperature. In large cells containing significant

energy (commercial spirally wound cells for example), this release of energy could generate enough heat to be a safety concern. Therefore, care should be taken when using this technique on full cells with significant energy content.

## STAR★METHODS

Detailed methods are provided in the online version of this paper and include the following:

## SUPPLEMENTAL INFORMATION

Supplemental information can be found online at https://doi.org/10.1016/j.isci.2021.103394.

## AUTHOR CONTRIBUTIONS

The manuscript was written largely by K.L.H with sections contributed by S.J.R. and D.M.L. The research plan was conceived by K.L.H. and K.L.J. B.W. fabricated and tested pouch cells. L.C.M. and S.G. disassembled pouch cells for characterization and prepared coin cells for characterization. D.M.L. and K.L.J. designed and performed cryo $Ga^+$ FIB/SEM experiments. S.J.R., J.C., K.L.J., and D.L.P. designed and performed cryo laser PFIB/SEM experiments. K.L.J colored the SEM images. S.A.R. and S.J.H. contributed data interpretation and analysis. All authors discussed the results, contributed to analyzing the data, and commented on or edited the manuscript.

## DECLARATION OF INTERESTS

We, a subgroup of authors, filed a patent application related to this work (application number 16/782,591) on February 5, 2020.

## REFERENCES

Aetukuri, N.B., Kitajima, S., Jung, E., Thompson, L.E., Virwani, K., Reich, M.L., Kunze, M., Schneider, M., Schmidbauer, W., and Wilcke, W.W. (2015). Flexible ion-conducting composite membranes for lithium batteries. Adv. Energy Mater. 5, 1500265.

Albertus, P., Babinec, S., Litzelman, S., and Newman, A. (2018). Status and challenges in enabling the lithium metal electrode for high-energy and low-cost rechargeable batteries. Nat. Energy 3, 16–21.

Albertus, P., and Newman, J. (2008). The Performance of Lithium-Ion Battery Cathodes Composed of Multiple Materials.ECS Meeting Abstracts (IOP Publishing), p. 1133.

Bach, T.C., Schuster, S.F., Fleder, E., Müller, J., Brand, M.J., Lorrmann, H., Jossen, A., and Sextl, G. (2016). Nonlinear aging of cylindrical lithium-ion cells linked to heterogeneous compression. J. Energy Storage 5, 212–223.

Biswal, P., Stalin, S., Kludze, A., Choudhury, S., and Archer, L.A. (2019). Nucleation and early stage growth of Li electrodeposits. Nano Lett. 19, 8191–8200.

Campbell, C., Lee, Y.M., Cho, K.Y., Lee, Y.-G., Lee, B., Phatak, C., and Hong, S. (2018). Effect of nanopatterning on mechanical properties of lithium anode. Sci. Rep. 8, 1–9.

Cannarella, J., and Arnold, C.B. (2014). Stress evolution and capacity fade in constrained lithium-ion pouch cells. J. Power Sources 245, 745–751.

Cho, J.H., Xiao, X., Guo, K., Liu, Y., Gao, H., and Sheldon, B.W. (2020). Stress evolution in lithium metal electrodes. Energy Storage Mater. 24, 281–290.

Ding, F., Xu, W., Chen, X., zhang, J., Engelhard, M.H., Zhang, Y., Johnson, B.R., Crum, J.V., Blake, T.A., and Liu, X. (2013). Effects of carbonate solvents and lithium salts on morphology and coulombic efficiency of lithium electrode. J. Electrochem. Soc. 160, A1894–A1901.

Ding, F., Xu, W., Chen, X., Zhang, J., Shao, Y., Engelhard, M.H., Zhang, Y., Blake, T.A., Graff, G.L., and Liu, X. (2014). Effects of cesium cations in lithium deposition via self-healing electrostatic shield mechanism. J. Phys. Chem. C 118, 4043–4049.

Eroglu, D., Zavadil, K.R., and Gallagher, K.G. (2015). Critical link between materials chemistry and cell-level design for high energy density and low cost lithium-sulfur transportation battery. J. Electrochem. Soc. 162, A982–A990.

Fang, C., Li, J., Zhang, M., Zhang, Y., Yang, F., Lee, J.Z., Lee, M.-H., Alvarado, J., Schroeder, M.A., and Yang, Y. (2019). Quantifying inactive lithium in lithium metal batteries. Nature 572, 511–515.

Fincher, C.D., Ojeda, D., Zhang, Y., Pharr, G.M., and Pharr, M. (2020). Mechanical properties of metallic lithium: From nano to bulk scales. Acta Mater. 186, 215–222.

Frenck, L., Sethi, G.K., Maslyn, J.A., and Balsara, N.P. (2019). Factors that control the formation of dendrites and other morphologies on lithium metal anodes. Front. Energy Res. 7, 115.

Gallagher, K.G., Goebel, S., Greszler, T., Mathias, M., Oelerich, W., Eroglu, D., and Srinivasan, V. (2014). Quantifying the promise of lithium–air batteries for electric vehicles. Energy Environ. Sci. 7, 1555–1563.

Gireaud, L., Grugeon, S., Laruelle, S., Yrieix, B., and Tarascon, J.-M. (2006). Lithium metal stripping/plating mechanisms studies: A metallurgical approach. Electrochem.Commun. 8, 1639–1649.

Han, H.-B., Zhou, S.-S., Zhang, D.-J., Feng, S.-W., Li, L.-F., Liu, K., Feng, W.-F., Nie, J., Li, H., and Huang, X.-J. (2011). Lithium bis (fluorosulfonyl) imide (LiFSI) as conducting salt for nonaqueous liquid electrolytes for lithium-ion batteries: Physicochemical and electrochemical properties. J. Power Sources 196, 3623–3632.

Harrison, K.L., Goriparti, S., Merrill, L.C., Long, D.M., Warren, B., Roberts, S.A., Perdue, B.R., Casias, Z., Cuillier, P., and Boyce, B.L. (2021). Effects of applied interfacial pressure on Li-metal cycling performance and morphology in 4 M LiFSI in DME. ACS Appl. Mater. Interfaces 13, 31668–31679.

Harrison, K.L., Zavadil, K.R., Hahn, N.T., Meng, X., Elam, J.W., Leenheer, A., Zhang, J.-G., and Jungjohann, K.L. (2017). Lithium self-discharge and its prevention: Direct visualization through in situ electrochemical scanning transmission electron microscopy. ACS Nano 11, 11194–11205.

He, Y., Ren, X., Xu, Y., Engelhard, M.H., Li, X., Xiao, J., Liu, J., Zhang, J.-G., Xu, W., and Wang, C. (2019). Origin of lithium whisker formation and growth under stress. Nat.Nanotechnol. 14, 1042–1047.

Herbert, E.G., Hackney, S.A., Dudney, N.J., and Phani, P.S. (2018). Nanoindentation of high-purity vapor deposited lithium films: The elastic modulus. J. Mater. Res. 33, 1335–1346.

Hirai, T., Yoshimatsu, I., and Yamaki, J.I. (1994a). Effect of additives on lithium cycling efficiency. J. Electrochem. Soc. 141, 2300–2305.

Hirai, T., Yoshimatsu, I., and Yamaki, J.I. (1994b). Influence of electrolyte on lithium cycling efficiency with pressurized electrode stack. J. Electrochem. Soc. 141, 611–614.

Jozwiuk, A., Berkes, B.B., Weiß, T., Sommer, H., Janek, J., and Brezesinski, T. (2016). The critical role of lithium nitrate in the gas evolution of lithium–sulfur batteries. Energy Environ. Sci. 9, 2603–2608.

Jungjohann, K.L., Gannon, R.N., Goriparti, S., Randolph, S.J., Merrill, L.C., Johnson, D.C., Zavadil, K.R., Harris, S.J., and Harrison, K.L. (2021). Cryogenic laser ablation reveals short-circuit mechanism in lithium metal batteries. ACS EnergyLett. 6, 2138–2144.

Kanamori, S., Matsumoto, M., Taminato, S., Mori, D., Takeda, Y., Hah, H.J., Takeuchi, T., and Imanishi, N. (2020). Lithium metal deposition/dissolution under uniaxial pressure with high-rigidity layered polyethylene separator. RSC Adv. 10, 17805–17815.

Kim, H., Jeong, G., Kim, Y.-U., Kim, J.-H., Park, C.-M., and Sohn, H.-J. (2013). Metallic anodes for next generation secondary batteries. Chem. Soc. Rev. 42, 9011–9034.

Klett, M., Eriksson, R., Groot, J., Svens, P., Högström, K.C., Lindström, R.W., Berg, H., Gustafson, T., Lindbergh, G., and Edström, K. (2014). Non-uniform aging of cycled commercial LiFePO$_4$//graphite cylindrical cells revealed by post-mortem analysis. J. Power Sources 257, 126–137.

Kozen, A.C., Lin, C.-F., Pearse, A.J., Schroeder, M.A., Han, X., Hu, L., Lee, S.-B., Rubloff, G.W., and Noked, M. (2015). Next-generation lithium metal anode engineering via atomic layer deposition. ACS Nano 9, 5884–5892.

Krauskopf, T., Hartmann, H., Zeier, W.G., and Janek, J.R. (2019). Toward a fundamental understanding of the lithium metal anode in solid-state batteries—an electrochemo-mechanical study on the garnet-type solid electrolyte Li$_{6.25}$Al$_{0.25}$La$_3$Zr$_2$O$_{12}$. ACS Appl. Mater. Interfaces 11, 14463–14477.

Kushima, A., So, K.P., Su, C., Bai, P., Kuriyama, N., Maebashi, T., Fujiwara, Y., Bazant, M.Z., and Li, J. (2017). Liquid cell transmission electron microscopy observation of lithium metal growth and dissolution: Root growth, dead lithium and lithium flotsams. Nano Energy 32, 271–279.

Lee, J.Z., Wynn, T.A., Schroeder, M.A., Alvarado, J., Wang, X., Xu, K., and Meng, Y.S. (2019). Cryogenic focused ion beam characterization of lithium metal anodes. ACS Energy Lett. 4, 489–493.

Li, F.S., Wu, Y.S., Chou, J., Winter, M., and Wu, N.L. (2015). A mechanically robust and highly ion-conductive polymer-blend coating for high-power and long-life lithium-ion battery anodes. Adv. Mater. 27, 130–137.

Li, L., Basu, S., Wang, Y., Chen, Z., Hundekar, P., Wang, B., Shi, J., Shi, Y., Narayanan, S., and Koratkar, N. (2018). Self-heating–induced healing of lithium dendrites. Science 359, 1513–1516.

Liao, J., and Ye, Z. (2018). Nontrivial effects of "trivial" parameters on the performance of lithium–sulfur batteries. Batteries 4, 22.

Lin, D., Liu, Y., and Cui, Y. (2017). Reviving the lithium metal anode for high-energy batteries. Nat. Nanotechnol. 12, 194–206.

Liu, J., Bao, Z., Cui, Y., Dufek, E.J., Goodenough, J.B., Khalifah, P., Li, Q., Liaw, B.Y., Liu, P., and Manthiram, A. (2019). Pathways for practical high-energy long-cycling lithium metal batteries. Nat.Energy 4, 180–186.

Liu, Y., Liu, Q., Xin, L., Liu, Y., Yang, F., Stach, E.A., and Xie, J. (2017). Making Li-metal electrodes rechargeable by controlling the dendrite growth direction. Nat.Energy 2, 1–10.

Louli, A., Eldesoky, A., Weber, R., Genovese, M., Coon, M., Degooyer, J., Deng, Z., White, R., Lee, J., and Rodgers, T. (2020). Diagnosing and correcting anode-free cell failure via electrolyte and morphological analysis. Nat.Energy 5, 693–702.

Louli, A.J., Genovese, M., Weber, R., Hames, S., Logan, E., and Dahn, J. (2019). Exploring the impact of mechanical pressure on the performance of anode-free lithium metal cells. J. Electrochem. Soc. 166, A1291–A1299.

Lu, J., Chen, Z., Pan, F., Cui, Y., and Amine, K. (2018). High-performance anode materials for rechargeable lithium-ion batteries. Electrochem.Energy Rev. 1, 35–53.

Mikhaylik, Y.V., Kovalev, I., Schock, R., Kumaresan, K., Xu, J., and Affinito, J. (2010). High energy rechargeable Li-S cells for EV application: Status, remaining problems and solutions. ECS Trans. 25, 23–34.

Mussa, A.S., Klett, M., Lindbergh, G., and Lindström, R.W. (2018). Effects of external pressure on the performance and ageing of single-layer lithium-ion pouch cells. J. Power Sources 385, 18–26.

Nadimpalli, S.P., Sethuraman, V.A., Abraham, D.P., Bower, A.F., and Guduru, P.R. (2015). Stress evolution in lithium-ion composite electrodes during electrochemical cycling and resulting internal pressures on the cell casing. J. Electrochem. Soc. 162, A2656–A2663.

Naoi, K., Mori, M., Naruoka, Y., Lamanna, W.M., and Atanasoski, R. (1999). The surface film formed on a lithium metal electrode in a new imide electrolyte, lithium bis (perfluoroethylsulfonylimide)[LiN($C_2F_5SO_2$)$_2$]. J. Electrochem. Soc. 146, 462–469.

Niu, C., Lee, H., Chen, S., Li, Q., Du, J., Xu, W., Zhang, J.-G., Whittingham, M.S., Xiao, J., and Liu, J. (2019). High-energy lithium metal pouch cells with limited anode swelling and long stable cycles. Nat.Energy 4, 551–559.

Ota, H., Shima, K., Ue, M., and Yamaki, J.-I. (2004). Effect of vinylene carbonate as additive to electrolyte for lithium metal anode. Electrochim. Acta 49, 565–572.

Peabody, C., and Arnold, C.B. (2011). The role of mechanically induced separator creep in lithium-ion battery capacity fade. J. Power Sources 196, 8147–8153.

Pei, A., Zheng, G., Shi, F., Li, Y., and Cui, Y. (2017). Nanoscale nucleation and growth of electrodeposited lithium metal. Nano Lett. 17, 1132–1139.

Petzl, M., Kasper, M., and Danzer, M.A. (2015). Lithium plating in a commercial lithium-ion battery–A low-temperature aging study. J. Power Sources 275, 799–807.

Qian, J., Henderson, W.A., Xu, W., Bhattacharya, P., Engelhard, M., Borodin, O., and Zhang, J.-G.

(2015). High rate and stable cycling of lithium metal anode. Nat. Commun. 6, 1–9.

Rodriguez, M.A., Harrison, K.L., Goriparti, S., Griego, J.J., Boyce, B.L., and Perdue, B.R. (2020). Use of a Be-dome holder for texture and strain characterization of Li metal thin films via $\sin^2(\psi)$ methodology. Powder Diffr. 35, 89–97.

Rubino, R.S., Gan, H., and Takeuchi, E.S. (2001). A study of capacity fade in cylindrical and prismatic lithium-ion batteries. J. Electrochem. Soc. 148, A1029–A1033.

Sanchez, A.J., Kazyak, E., Chen, Y., Chen, K.-H., Pattison, E.R., and Dasgupta, N.P. (2020). Plan-view operando video microscopy of Li metal anodes: Identifying the coupled relationships among nucleation, morphology, and reversibility. ACS EnergyLett. 5, 994–1004.

Schweikert, N., Heinzmann, R., Eichhöfer, A., Hahn, H., and Indris, S. (2012). Electrochemical impedance spectroscopy of $Li_4Ti_5O_{12}$ and $LiCoO_2$ based half-cells and $Li_4Ti_5O_{12}/LiCoO_2$ cells: Internal interfaces and influence of state-of-charge and cycle number. Solid State Ionics 226, 15–23.

Sun, C., Liu, J., Gong, Y., Wilkinson, D.P., and Zhang, J. (2017). Recent advances in all-solid-state rechargeable lithium batteries. Nano Energy 33, 363–386.

Takada, K. (2013). Progress and prospective of solid-state lithium batteries. Acta Mater. 61, 759–770.

Tarascon, J.-M., and Armand, M. (2001). Issues and challenges facing rechargeable lithium batteries. Nature 414, 359–367.

Verma, A., Kawakami, H., Wada, H., Hirowatari, A., Ikeda, N., Mizuno, Y., Kotaka, T., Aotani, K., Tabuchi, Y., and Mukherjee, P.P. (2021). Microstructure and pressure-driven electrodeposition stability in solid-statebatteries. Cell Rep. Phys. Sci. 2, 100301.

Wang, H., Huang, W., Yu, Z., Huang, W., Xu, R., Zhang, Z., Bao, Z., and Cui, Y. (2021). Efficient lithium metal cycling over a wide range of pressures from an anion-derived solid-electrolyte interphase framework. ACS EnergyLett. 6, 816–825.

Wang, M.J., Choudhury, R., and Sakamoto, J. (2019). Characterizing the Li-solid-electrolyte interface dynamics as a function of stack pressure and current density. Joule 3, 2165–2178.

Weber, R., Genovese, M., Louli, A., Hames, S., Martin, C., Hill, I.G., and Dahn, J. (2019). Long cycle life and dendrite-free lithium morphology in

anode-free lithium pouch cells enabled by a dual-salt liquid electrolyte. Nat.Energy 4, 683–689.

Wilkinson, D., Blom, H., Brandt, K., and Wainwright, D. (1991). Effects of physical constraints on Li cyclability. J. Power Sources 36, 517–527.

Wilkinson, D., and Wainwright, D. (1993). In-situ study of electrode stack growth in rechargeable cells at constant pressure. J. Electroanal. Chem. 355, 193–203.

Xu, C., Ahmad, Z., Aryanfar, A., Viswanathan, V., and Greer, J.R. (2017). Enhanced strength and temperature dependence of mechanical properties of Li at small scales and its implications for Li metal anodes. PNAS 114, 57–61.

Yin, X., Tang, W., Phua, K.C., Adams, S., Lee, S.W., and Zheng, G.W. (2018). Insights into morphological evolution and cycling behaviour of lithium metal anode under mechanical pressure. Nano Energy 50, 659–664.

Zachman, M.J., Tu, Z., Archer, L.A., and Kourkoutis, L.F. (2020). Nanoscale elemental mapping of intact solid–liquid interfaces and reactive materials in energy devices enabled by cryo-FIB/SEM. ACS EnergyLett. 5, 1224–1232.

Zachman, M.J., Tu, Z., Choudhury, S., Archer, L.A., and Kourkoutis, L.F. (2018). Cryo-stem mapping of solid–liquid interfaces and dendrites in lithium-metal batteries. Nature 560, 345–349.

Zhang, S.S. (2006). A review on electrolyte additives for lithium-ion batteries. J. Power Sources 162, 1379–1394.

Zhang, X., Wang, Q.J., Harrison, K.L., Jungjohann, K., Boyce, B.L., Roberts, S.A., Attia, P.M., and Harris, S.J. (2019). Rethinking how external pressure can suppress dendrites in lithium metal batteries. J. Electrochem. Soc. 166, A3639–A3652.

Zhang, X., Wang, Q.J., Harrison, K.L., Roberts, S.A., and Harris, S.J. (2020). Pressure-driven interface evolution in solid-state lithium metal batteries. Cell Rep. Phys. Sci. 1, 100012.

Zhao, Y., Patel, Y., Hunt, I.A., Kareh, K.M., Holland, A.A., Korte, C., Dear, J.P., Yue, Y., and Offer, G.J. (2017). Preventing lithium ion battery failure during high temperatures by externally applied compression. J. Energy Storage 13, 296–303.

Zheng, G., Lee, S.W., Liang, Z., Lee, H.-W., Yan, K., Yao, H., Wang, H., Li, W., Chu, S., and Cui, Y. (2014). Interconnected hollow carbon nanospheres for stable lithium metal anodes. Nat. Nanotechnol. 9, 618–623.

# STAR★METHODS

## KEY RESOURCES TABLE

| REAGENT or RESOURCE | SOURCE | IDENTIFIER |
|---|---|---|
| Chemicals, peptides, and recombinant proteins | | |
| 1,2 dimethoxyethane | Sigma-Aldrich | 259527 |
| Lithium bis(fluorosulfonyl)imide | Oakwood Chemicals | 097602 |
| Lithium (50 μm) on copper (10 μm) | Albemarle | 402064600 |
| Hydrochloric acid | Sigma-Aldrich | 320331 |

## RESOURCE AVAILABILITY

### Lead contact

Further information and requests for resources should be directed to and will be fulfilled by the lead contact, Katharine L. Harrison (katharr@sandia.gov).

### Materials availability

This study did not generate new reagents.

### Data and code availability

- Data reported in this paper will be shared by the lead contact upon request.

- This paper does not report original code.

- All additional information required to reanalyze the data reported in this paper is available from the lead contact upon request.

## METHOD DETAILS

### Electrolyte preparation

4 M LiFSI in DME was prepared as has previously been documented (Qian et al., 2015) by mixing 1,2 dimethoxyethane (DME) and lithium bis(fluorosulfonyl)imide (LiFSI) in a 1.4:1 molar ratio (DME:LiFSI) in an Ar-filled glove box. Before mixing the salt and solvent, DME (Sigma-Aldrich, anhydrous, 99.5%) was dried over activated alumina for at least two days such that the volume of activated alumina:DME was approximately 1:4. Before adding the DME, the activated alumina was prepared by drying for at least two days at 200°C under vacuum in the glove box antechamber. To remove the activated alumina from the DME, the DME was extracted through a filter. The LiFSI salt (Oakwood Chemicals) was also dried under vacuum in a heated glove box antechamber at 100°C overnight before adding it to the solvent. The DME and LiFSI solution was then stirred overnight on a hot plate at 50°C.

### Pouch cell fabrication

Pouch cell fabrication schematics are provided elsewhere (Harrison et al., 2021) but the details regarding fabrication are provided here. 20 μm thick Cu current collectors were used as the working electrodes. They were first etched with 1.2 M hydrochloric acid for 10 min and then quickly rinsed with deionized water and acetone and dried with Kimwipes before transferring to an Ar-filled glove box. 50μm thick Li on 10 μm thick Cu (Albemarle) were used as received for counter/reference electrodes. The electrodes were punched using a custom die into 1.25″ diameter circles with a connected lead. The counter electrode was punched such that only the circle consisted of Li on Cu and the lead consisted of bare Cu. Pre-taped Ni leads (Pred Materials) were spot welded to the Cu leads on the punched electrodes. Polymer-coated aluminum (Pred Materials) was prepared with depressions to serve as the pouch cell packaging. The depressed pouch was larger than the 1.25″ diameter stack to ensure that any gas that formed in pressurized cells would not lead to rupture (though no gas formation was observed). Pouch cells were then fabricated in a dry room with an average dewpoint of −55°C using Pred Materials equipment by placing two sheets of Celgard 2325 separator (55x45 mm to fit in the pouch depressions) between the electrodes and aligning with a

jig. In some cells only one sheet of Celgard 2325 separator was used, as is clearly indicated in the text and figures throughout the manuscript. Three sides were sealed and then 1 mL of 4 M LiFSI in DME was pipetted into the cell between the two separator sheets or on both sides of the separator when only one sheet was used. This quantity was sufficient to flood the cell with excess electrolyte and excess electrolyte could spread outside of the pressurized stack. After the electrolyte was added, the final side was sealed under vacuum.

### Applying interfacial pressure to pouch cell batteries

Uniaxial pressure was applied to pouch cells normal to the electrode-electrolyte interfaces using a variety of instruments appropriate for applying pressure across 5 orders of magnitude. Photographs of the apparatuses for applying pressure are provided elsewhere (Harrison et al., 2021) but procedures for applying pressure are summarized here. Cells cycled at 0 MPa were placed on a leveled stage and tested without any pressure applied to the cell. Cells cycled at 0.01 MPa were tested with dead weights to provide constant force. Cells cycled at 0.1 MPa were pressurized by dead weights or a Sandia-built four-station pneumatic pressure tester designed for testing pouch cells under constant force, controlled to $\sim$0.5 lb precision using proportional, integral, derivative (PID) feedback control. Cells cycled at 1 MPa were tested with an MTI Corporation YLJ-HP80 pneumatic press and by hydraulic or electromechanical load frames. Cells cycled at 10 MPa were tested by hydraulic or electromechanical load frames. The four-station tester, the MTI press, and the load frames all were equipped with feedback control to keep the pressure constant during cycling rather than applying the set pressure initially and keeping the platen gap spacing constant. Custom-machined, mirror-bright platens on leveled stages were used to minimize roughness and apply pressure uniformly to the pouch.

### Electrochemical testing

All cells were cycled with Gamry 1000E and 1010E potentiostats at a current density of 4 mA/cm$^2$ to a capacity of 2 mAh/cm$^2$. Deposition steps were terminated by a time limit to enable a constant deposition capacity. However, a voltage limit of $-1$ V was also used as a cut off in case the cell polarized before reaching the programmed capacity. Stripping steps were terminated with a 1 V limit to enable the detection of parasitic stripping current that might arise from a shorted cell. However, to prevent stripping steps from infinitely passing current in the event of a short circuit, a time limit was also set such that stripping steps would terminate at the time equivalent to double the programmed plating capacity. Electrochemical impedance spectroscopy (EIS) tests were performed prior to cycling and after each deposition step. A 5 min open circuit rest period was applied before running EIS to allow for the potential to stabilize. EIS tests were performed with a 5 mV rms AC voltage perturbation ranging from 0.02 Hz to 1 MHz. Cells were cycled and stopped either after one deposition (for characterization) or after 51 plating steps and 50 stripping steps. CE of a given cycle refers to the percentage of capacity passed during the plating step that is recovered during the stripping step as defined by Equation 1. The cumulative average CE (CE$_{CA}$) of a given cycle refers to the total capacity passed during all stripping steps up to and including the cycle in question summed together and divided by the sum of total capacity passed during all plating steps up to and including the cycle in question and then multiplied by 100%. CE$_{CA}$ is defined by Equation 2.

$$(CE)_{cycle\ x} = 100\% * \frac{(stripping\ capacity)_{cycle\ x}}{(plating\ capacity)_{cycle\ x}} \qquad \text{(Equation 1)}$$

$$(Cumulative\ Average\ CE)_{cycle\ x} = 100\% * \frac{\sum_{n=1}^{n=x}(stripping\ capacity)_{cycle\ n}}{\sum_{n=1}^{n=x}(plating\ capacity)_{cycle\ n}} \qquad \text{(Equation 2)}$$

### Pouch cell disassembly and electrode extraction for Ga$^+$FIB milling and SEM imaging

After 1 deposition on the working electrode (one half cycle), pouch cells were disassembled in an Ar-filled glove box. A razor blade was used to cut the first layer of the pouch bag material on three sides outside of the electrode stack without cutting through the separator. The resulting flap was then raised, and the counter electrode was removed by cutting the lead. Subsequently, the separators and working electrode were removed. Before ex-situ characterization, the electrodes were soaked in dry DME for 30 s to remove excess electrolyte.

## Ex-situ cryo Ga⁺FIB milling and SEM imaging

Cryo Ga$^+$ FIB and SEM were used to cross-section and image the deposits on the working electrodes after one deposition. The electrodes were extracted as described above and pieces were mounted on SEM stubs in an Ar-filled glove box. The electrodes were transferred from the glove box in sealed jars and frozen in a cryo bath. The samples were secured on a cryo mount under liquid nitrogen and then sputter coated with 10 nm of Pt at −160°C. Then they were transferred to a Thermo Fisher Scientific Scios 2 under high vacuum conditions onto a Leica cryo-stage held at −150°C. The electrodes were imaged at 5 kV and 50 pA initially before selecting a representative region to mill with Ga$^+$ at 16 kV and 1–15 nA. The milled cross-sections were then polished and imaged at 5 kV and 50 pA.

## Pouch cell disassembly and coin cell fabrication for cryo laser PFIB milling and SEM imaging

Pouch cells are very large relative to the cryo stage in the laser PFIB/SEM, so entire pouch cells could not be kept cold on the cryo stage to enable direct cross-sectioning and imaging of the electrode stacks inside of the pouch cells. Instead, the pouch cells were disassembled and rebuilt into coin cells for the cryo laser PFIB/SEM characterization. The pouch depressions were cut with a razor blade on three sides to allow access to the electrode stack. Then the lead on the counter electrode was cut, followed by the working electrode, so that entire stacks could be removed from the pouch cells. Sections of entire stacks were then cut out using insulating, ceramic scissors and placed in coin cell cases, enabling air-free transfer to the SEM.

## Cryo laser PFIB milling and SEM imaging

All cryogenic laser processing was performed in a prototype of the Thermo Fisher Scientific Helios Laser PFIB, which is comprised of electron, ion, and femtosecond (fs) pulsed laser beams, all focused to a single point in space under high vacuum allowing high rate, low damage material removal and imaging. The fs laser is necessitated for this process as the analysis of intact coin cells requires removal of hundreds of µm of stainless steel before reaching the active area, a process that becomes time prohibitive by PFIB alone. The ultrashort pulse provides ample energy for this amount of material removal, while minimizing the thermal load on the delicate Li metal, frozen electrolyte, and polymer separators.

The laser PFIB was modified with a cryogenic cooling stage as required for this work. In order to accommodate these samples, we designed a custom cryo pretilt holder capable of securely holding the devices with the coin cell case sides isolated and the top surface grounded to reduce charging. The pre-tilted wedge was fabricated from copper with a recessed pocket to hold the coin cell flush with the top surface of the holder. The electrical isolation was ensured by placing an insulating polyimide disk at the base of the recess on which the cathode cap in the coin cell is curved to seal. A pretilt of −26° (angled toward the laser and away from FIB) was chosen due to geometrical constraints in the system. The prototype version of this tool has access to an additional −10° of stage tilt, so the maximum sample tilt toward the laser is −36°. The laser was positioned such that normal incidence occurs at −60°, so all laser processing was done at an oblique angle with the steepest cut face being nominally 24° off-normal after final polishing.

Prior to loading an individual coin cell into the holder, it was cooled to cryogenic temperatures. Through experiment we found that the most effective way to cool the cell, without causing thermally induced cracking internally, was through slow cooling to operating temperatures. To slow the heat transfer, we placed the coin cell inside of two nested pyrex beakers which were then placed into a liquid nitrogen bath for 10–15 min. This resulted in a slowed cooling rate of the coin cell, after which it could be placed directly in liquid nitrogen for 10–15 min to reach ultimate temperature. Working quickly with cooled tweezers, we then transferred the frozen cell to the pre-cooled cryo stage with the custom holder (mounted to stage and pre-cooled also) and secured it via grounded clamping screws. The system was then immediately evacuated to minimize condensation and frost formation, although this was rarely problematic. This transfer in air did result in a rise in temperature of the stage and the cell, even when working quickly. However, the stage and cell were allowed to reach at least −150°C and then we waited an additional 10 min prior to the first laser cuts. The additional cooling time was a precaution to ensure the entire cell was at cryo temperature before cutting.

Laser sectioning was typically performed in three successive steps with the final step being somewhat variable depending upon the active region morphology and thickness. First, coarse cutting was performed with a stage tilt of −5° using box mill and parameters given in the laser control user interface. Then the stage was offset approximately 100 µm in the y-direction to remove the section of material from the cut

face that is roughened from coarse milling. Next, a second cutting step was performed with an additional degree of negative tilt. The instrument was then vented to replace the coverslip that was used to protect the microscope from milling debris. During this step, the samples were exposed to air, though they remained frozen on the cryo stage, so reactivity remained minimal. Condensation sometimes led to ice formation on the samples during the air exposure related to this step, but air exposure and the related condensation could be eliminated by the use of a glove bag around the SEM during the slide change step. The final step required a change of wavelength and again steepened the cut face angle by increasing the negative tilt of the stage. We used the shorter wavelength for the final polish as it reduced the laser-induced periodic surface structure artifacts and resulted in higher quality images. The additional negative tilt applied at the final polish (from −7° to −10°) offered the advantage of being able to locate the laser beam precisely at the interface between the steel and the active area. In this manner, the lower pulse energy (515 nm) beam did not need to cut through the entire steel casing and the beam and patterning parameters could be tailored to only address the important active area. This final polishing step had to be adjusted slightly around the nominal conditions discussed here, depending on the sample morphology. Typically, the critical parameters that were adjusted were the number of pulses per pixel delivered, the total passes scanned, and changing polarization. Most other parameters were less impactful to the final result. The nominal conditions used for most samples are summarized in Table S1.

Finally, imaging was then carried out in the desired SEM modes; however, we generally used backscatter imaging due to reduced susceptibility to charging and for its material contrast advantages. Beam energies for imaging were typically 1–3 keV with 1 keV being the best balance between charge control and image contrast. Imaging at 2–3 keV typically resulted in improved contrast of Li, which appeared dark in backscatter images, but sacrificed charge control in the electrolyte and separator layers.